Theses and Dissertations

Spring 2014

Micro-bending and patterning via high energy pulse laser peening

Chelsey Nicole Pence
University of Iowa

Recommended Citation

MICRO-BENDING AND PATTERNING VIA HIGH ENERGY PULSE LASER

PEENING

by

Chelsey Nicole Pence

A thesis submitted in partial fulfillment
of the requirements for the Master of
Science degree in Mechanical Engineering
in the Graduate College of
The University of Iowa

May 2014

Thesis Supervisor: Assistant Professor Hongtao Ding

Graduate College
The University of Iowa
Iowa City, Iowa

CERTIFICATE OF APPROVAL

_____

MASTER'S THESIS

_____

This is to certify that the Master's thesis of

Chelsey Nicole Pence

has been approved by the Examining Committee
for the thesis requirement for the Master of Science
degree in Mechanical Engineering at the May 2014 graduation.

Thesis Committee: _____
                  Hongtao Ding, Thesis Supervisor

                  _____
                  Hiroyuki Sugiyama

                  _____
                  Shaoping Xiao

To my family: Mom, Dad, Hayley, Casey, Chloe, and Joe.

ACKNOWLEDGMENTS

I would like to thank my advisor, Professor Hongtao Ding, for encouraging me to participate in research opportunities at the University of Iowa, and also his knowledge and guidance throughout the entire process of research and writing this thesis. I would also like to thank Ninggang Shen being not only a great mentor, but also a friend. I would also like to thank Andrea Flaherty for her continuous help throughout my years at the University of Iowa.

In addition, I would like to think Robert Bowers, Yin Yu, Dr. Clark Stanford, and Professor Ibrahim Ozbolat for their help in my research of improving cell-attachment on bio-implant materials, and Dr. Justin Garvin for his help with hydrodynamic modeling.

Last, but certainly not least, I would like to thank my family, the most loving, supporting people I know, for always believing in me as I pursued my dreams for a higher education. Without them I would not be the person I am today. Finally, I would like to thank Joe for his love and encouragement as I finished this final year of my educational career.

ABSTRACT

High energy pulse laser peening (HEPLP) is a manufacturing process, in which a strong shock wave is produced and induces high pressures on the surface of the target material. Generally, this process is used to improve material properties such as the hardness and fatigue life. First a 2D multi-physics model for the process was investigated, which simulates the pressure induced on the surface of the target material. The model can be coupled with commercial finite element software, such as ABAQUS, to more accurately simulate the HEPLP process to find stresses and deformations on the surface. Next two novel applications using the HEPLP process were investigated.

The first, laser shock bending is a sheet metal micro-forming process using HEPLP to accurately bend, shape, precision align, or repair micro-components with bending angles less than 10°. Negative bending angle (away from laser beam) can be achieved with the high-energy pulsed laser, in addition to the conventional positive laser bending mechanism. In this thesis, various experimental and numerical studies on aluminum sheets were conducted to investigate the different deformation mechanisms, positive and negative. The experiments were conducted with the sheet thickness varying from 0.25 to 1.75 mm and laser pulse energy of 0.2 to 0.5 J. A critical thickness threshold of 0.7-0.88 mm was found that the transition of positive negative bending mechanism occurs. A statistic regression analysis was also developed to determine the bending angle as a function of laser process parameters for positive bending cases.

The second application studied used HEPLP to imprint complex two-dimensional (2D) patterns dental implant material of cpTi. Pure titanium (commercial pure cpTi) is an ideal dental implant material, without the leeching of toxic alloy elements. Evidence has shown that unsmooth implant surface topologies may contribute to the osteoblast differentiation in human mesenchymal pre-osteoblastic cells, which is helpful to avoid long-term peri-abutment inflammation issues for the dental implant therapy with transcutaneous devices. Studies have been conducted on the grit blasted, acid etched, or

uni-directional grooved Ti surface, however, for these existing approaches the surface quality is difficult to control or may even damage the implant. The strong shock wave generated by HEPLP is used to press a stainless steel grid, used as a stamp, on Ti foils to imprint a 2D pattern. In this study, the multiple grid patterns and grid sizes were applied to test for cell-attachment improvements. Then, the cell culture tests were conducted with the patterned surface to investigate the contribution of these 2D patterns, with the control tests of the other existing implant surface topography forming approaches. The micro-patterns proved successful in increasing the cell-attachment, increasing the number of cells attaching to the material and also contributing to the cell-growth within the grooved areas.

v

TABLE OF CONTENTS

LIST OF TABLES

Table

viii

LIST OF FIGURES

Figure

ix

CHAPTER I

INTRODUCTION

High energy pulse laser peening (HEPLP) is a manufacturing process shown to improve material properties such as the hardness and fatigue life. The process consists of short laser pulses of 6-8 nanoseconds, focused to explode an ablative coating, which result in a high pressure shock wave with a peak pressure of 2-10 GPa [1,2]. The laser-induced high pressure shock wave then propagates into the substrate material, generating plastic deformation with a compressive layer as deep as about 1 mm [3]. The compressive stress induced on the surface refines the grain structure, enhancing the material properties. In this work, two novel techniques, which use the HEPLP process for more than simply enhancing material properties, are investigated. The first implements the HEPLP technique as a non-contact sheet metal forming method and the other to create micro-patterns on the surface of bio-implant material in order to improve cell-attachment. One key component to any research of this nature is modeling, which can be used to understand important process parameters and optimize the technique. For this, a physics-based hydrodynamic model developed by Wu & Shen [4] was adopted to predict the pressure induced by the shock wave created by the laser pulse. The pressures from these simulations could then be entered into a finite element analysis (FEA) program, such as ABAQUS, to predict the stresses and deformation. Below outlines the objectives of this research and the order in which it will be presented.

Research Objectives and Outline

The objectives of this study are to develop an understanding of the HEPLP process, how it can be modeled, and two applications. First, a review of each of the aforementioned topics are given in Chapter II. Chapter III is a study of the multi-physics based model used to predict the pressure induced on the surface of the target material, which can then be used for FEA. Chapters IV and V investigate two novel applications for the HEPLP process,

sheet metal bending and surface patterning of bio-implants. Chapters V also shows how the model discussed in Chapter III can be used to for more accurate FE modeling.

CHAPTER II

LITERATURE REVIEW

High Energy Pulse Laser Peening

High energy pulse laser peening (HEPLP), an innovative laser surface treatment process, is a manufacturing technique that has been shown to improve surface corrosion resistance, mechanical strength, and fatigue performance. During the process, a powerful pulse laser beam with power intensities above 1 GW/cm^2 is focused to peen the target material surface. A translucent layer, usually consisting of flowing water or glass, is employed over the surface and acts as a confinement layer, as shown in Figure 1. Short laser pulses with a time period of about 10 nanoseconds are focused to explode the ablative coating. The shock wave is confined by the confinement layer, then propagates into the substrate material and results in a high pressures, with a peak pressure of 1-10 GPa induced on the surface [1–3,5,6].
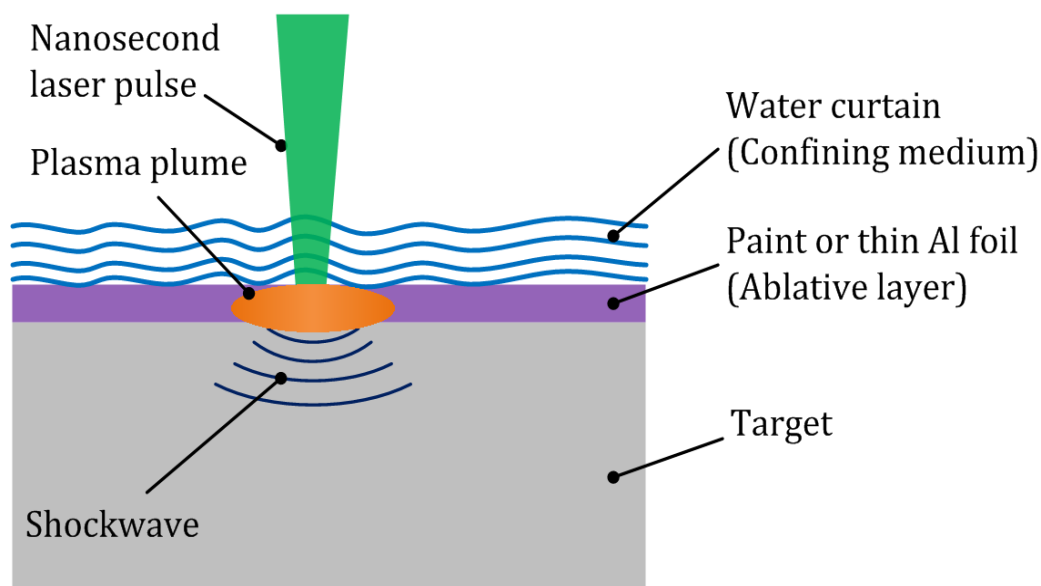
Figure 1. Laser-induced shockwave schematic

The high pressure shock wave directed into the target material generates plastic deformation with a compressive layer as deep as 1 mm [3], which refines grain structure and strengthens the material. In metals, grain size significantly influences the mechanical properties; large grain size is generally associated with low strength, low hardness, and low corrosion resistance, hence refining grain size can improve these material qualities. In the case of pure titanium, for example, multiple studies have shown that by decreasing the grain size to submicron level, the corrosion rate can be reduced by as much as 50% and the mechanical strength can be increased by 30-40% [7–12]. While there are other methods to decrease grain size, conventional techniques will not work for applications with complex geometries and a high demand for precision.

Moving forward, modeling is needed to predict the pressures and residual stresses induced on the surface of the target material during the HEPLP process. In the next section, physics-based models for the process are reviewed.

Multi-Physics Modeling of Laser Shockwaves

For finite element analysis of the laser peening process, it is critical to know the shock pressure that will be induced on the surface to have an accurate model. For this reason, a model to predict the shockwave pressure induced by the laser-matter interaction would be of great use and has been in development in the recent years. Models have been developed to not only predict the pressure, but also the velocity, temperature, stress, and energy distributions at the coating-confinement layer interface. A model proposed by Fabbro et al. [13] has been widely used in laser peening numerical analyses, in which two free variables are used to make predictions such as indentation profile and residual stress [14–18].

Wu and Shin have developed a self-closed thermal model for the confined plasma in the laser peening process, considering most of the important and relevant physical processes, without using any free variables. Cao et al. [3] applied the confined plasma

model from Ref. [19] coupled with finite element analysis to accurately predict the indentation profile and residual stresses on various metallic target specimens, such as 4140 steel, 316L stainless steel and Ti6Al4V alloy, for peening under various laser conditions.

More recently, Wu and Shin [19] have developed a numerical model with more strict physics considerations, where the hydrodynamic governing equations of conservation of mass, momentum, and energy of the confining medium and metal targets are used along with the appropriate equations of state. Both one and two-dimensional models have been developed and can be chosen depending on the laser beam diameter. The two-dimensional model is similar to the ones developed in Ref. [1] and Ref. [43], but predicts the axisymmetric spatial distribution, in both the radial direction and the depth, of induced pressures due to plasma expansion near the coating-water interface. For laser beam diameter less than 1 mm, the radial expansion of plasma can be neglected and hence the one-dimensional model can be used [4]. The ultimate goal of this analysis is to calculate the pressures induced near the water-coating interface, which can then be entered into a finite element model as the surface load to obtain residual stresses and deformation in the work-piece target material [19]. Furthermore, the numerical model can be used to design experiments, predict results, and further analyze results found in physical experiments.

After studying the phenomena of HEPLP and the models that can be used to predict the pressure induced through the process, two separate applications using the HEPLP process were investigated.

Applications

In this section the two applications studied in this work, sheet metal bending and patterning for bio-applications using the HEPLP process, are reviewed.

Sheet Metal Micro-Bending

Industries such as aerospace, automotive, ship building, and microelectronics currently bend sheet metal using expensive stamping dies and presses for prototype

evaluations. Using these conventional methods, however, complex three-dimensional (3D) features are difficult or impossible to attain [20,21]. As a possible solution to this problem, a non-contact forming method in which sheet metals can be bent, shaped, and precision-aligned using straight or curved laser scan lines, has been studied. Using this process, 3D features that were previously difficult to attain can be achieved. Conventionally, the laser bending process uses a focused laser beam and irradiation to introduce thermal stress on the work piece. The three types of material bending mechanisms by laser thermal forming technologies, temperature gradient mechanism, buckling mechanism, and upsetting mechanism [22], consider both specimen geometries and laser process conditions. The deformations in the thermal forming process happens because of the partial restraint to thermal expansion in the heated area from the ambient colder material. Due to the thermal expansion and shrinkage, stresses in the component are induced and then by distortions and stress redistributions, balance themselves [23].

As opposed to the thermal laser forming process, non-thermal forming using a high-energy pulsed laser has generated growing interest. The process is similar to mechanical shot peening, a process in which the target surface is impacted with a high velocity stream of hard particles. The force from the impacting particles produces a compressive residual stress on the surface and in turn modifies the mechanical properties [24]. The difference between shot peening and laser peening, however, is that instead of impacting the surface with solid particles, the laser peening process uses high-energy laser pulses to induce high pressures and compressive shockwaves onto the target material. During the process, short laser pulse irradiation duration, on the order of nanoseconds, is required, which is several-orders less than the radiation time of the thermal forming mechanism [2]. In order to have plastic deformation, the peak pressure of the shock wave induced by the laser at the surface of the sheet must be greater than the dynamic yield strength of the material [25,26]. The

yield region will experience residual stress and the sheet metal will bend to balance the stress.

To fully understand the laser bending process, modeling is crucial. The ability to model and accurately control the bending angle of the sheet metal during the process will also be necessary to implement the laser bending technique in industry. Many aspects of the process play critical roles in determining the bending angle, including; laser parameters, scanning scheme, and target materials. Both experimental and numerical analyses have been conducted to predict the bending angle produced during the laser sheet metal bending process.

A numerical study of the effects of scanning schemes on bending angle, distortions, and stress distribution in laser tube bending was presented by Safdar et al. [27], in which it was shown that scanning schemes significantly influence laser tube bending. For the given process parameters, the axial scanning scheme was shown to produce a bending angle twice that as obtained by circumferential scanning schemes. Wielage and Vollertsen [28] investigated was role the deformation velocity of laser shock forming plays on the length of the bent sample. The experiments were conducted using a TEA-CO_2-laser pulsed with a pulse duration of 100 ns, a wavelength of 10.6 μm, and laser shock wave pressure up to 5.6 MPa per pulse.

Shidid et al. [29] studied how flow conditions, inert gas combinations, nozzle positions, and gas shielding effects laser bending of titanium sheet metal using a 550W multimode Nd:YAG laser system. It was shown that gas flow conditions, nozzle positions, and inert gas combinations could be used to enhance the bending angle and quality.

Both numerical and experimental investigations were performed by Shen et al. [23] to analyze the edge effects when bending low carbon steel using the straight line laser bending process with a 3 kW CO_2 laser. They found that the scanning schemes significantly influence the bending angle distribution along the scan line, and by accelerating and

decelerating the scanning schemes the edge effects can be minimized. The relationship between laser process parameters and bending angle can be described using derived empirical formulas [6].

Maji et al. [30] conducted experimental and statistical analyses of bending of AISI 304 stainless steel sheets using a pulsed 2-kW fiber laser, where the statistical analysis was used to study the effects of process parameters of laser power, scan speed, spot diameter and pulsed duration on bending angle. Gollo et al. [29,31] conducted laser bending experiments with 1-mm-thick mild steel AISI 1010 using a pulsed Nd:YAG laser with maximum mean laser power of 400 W and applied the process to control micro-component adjustments. The regression analysis showed the influence process parameters, including material laser power, beam diameter, scan velocity, sheet thickness, pass number, and pulse duration, on bending angles.

Geiger and Meyer-Pittroff [32] showed how laser forming could be used for high precision manipulation of functional electronic and optical devices. According to Dearden and Edwardson [33] precision alignment is currently part of the process during product assembly for microscale applications. Zhang and Xu [34] first investigated the adjustment of curvatures of silicon micro-cantilevers using a pulsed frequency doubled Nd:YLF laser with a wavelength of 524 nm, pulse duration of 20 ns, and pulse energies of 0.18 to 0.32 μJ. In addition, Zhang and Xu [35] studied the high precision microscale laser bending technique by performed a three-dimensional finite element analysis on laser bending of a hard disk suspension.

Currently, most work on laser bending has been focused on bending the sheet metal towards the laser beam (positive bending) using thermal forming techniques, while little has been studied on producing a bend that moves away from the laser beam (negative bending) [6]. Even less research has been done on producing this negative bending angle with the use of a high-energy pulsed laser, rather than by using the thermal effects of the

laser beam to produce the bend [6]. Liu et al. [20] and Guan et al. [21] experimentally investigated how to produce negative bending angles on stainless foil by way of laser bending using a 50W American Synrad 48-5 series CO_2 laser with a wavelength of 10.6 μm. They were able to produce negative bending angles when the elastic pre-bending was induced in a direction away from the laser beam.

Although the research presented by Liu et al. [20] and Guan et al. [21] gave initial guidance on pretreatment of the specimen and process parameter optimization to produce negative bending, many other issues were further addressed in the study presented. For example, during the laser micro-bending process, it would be extremely difficult to deposit absorptive coatings frequently, and also how to effectively remove the coating later. There has also been few studies showing how to simply and accurately control the bending angle. In this study, various laser bending experiments were conducted on thin aluminum sheets in a one-side shock configuration using a nanosecond Nd:YAG pulse laser to address how to control the deformation technique in laser micro-bending [6]. Usually the problems seen in assembly processes must be corrected with a bending angle of 10° or less, so this was the focus of the study. The research looked at the effects of various parameters on the laser micro-bending process, including; laser pulse energy, scanning scheme, and sheet thickness. The positive or negative bending mechanisms were then analyzed using finite element (FE) in ABAQUS.

Micro-Surface Patterning for Bio-Applications

Micro-surface patterning is currently being used for the fabrication of advanced technologies, such as the fabrications of micro-electro-mechanical systems (MEMS), and nanoscale sensors and actuators. However, evidence has shown that patterning could also improve the functionality for bio-applications, such as commercially pure titanium (cpTi) dental implants [36–38]. One major issue is that producing patterns on the surface of metals has proven to be very difficult because of the high hardness of the material.

Conventional methods for producing micro-patterns on metal materials are etching-related, and have disadvantages of high environmental impact and low reproducibility. Recently, Ye and Cheng [5] proposed a new method, in which they produced patterned micro-indents on the surface of NiTi shape memory alloy using laser shock assisted direct imprinting. The technique uses the plasma pressure generated from the laser shock to punch a mask into the target material, generating patterned indents from the punched mask.

The technique used by Ye and Cheng was then adopted for the investigation in this thesis, which aimed to improve the cell-attachment on dental implants by creating micro-patterns on surface of the material. Without proper cell-attachment, chronic inflammation due to the lack of tissue growth around the implant device can occur, which can lead to the potential for mucosal recession or even implant loss. Studies have shown that when comparing rough versus grooved surfaces, cells align with the grooves on the grooved surface, and similarly with the pattern found on the rough surface [36,37,39,40]. Existing approaches used to create roughened or patterned implant surfaces are grit blasting, acid etching, or uni-directional grooving of Ti surfaces, however these can damage the implant and the surface quality is very difficult to control.

CHAPTER III

MULTI-PHYSICS MODELING OF LASER SHOCKWAVES

Introduction

In this chapter, a multi-physics model developed by Wu & Shin [4] for the HEPLP process was studied and adopted for the laser parameters used in experimental studies of laser peening applications and then used to perform an accurate finite element (FE) analysis in ABAQUS for the studies in Chapter IV and V. The numerical model calculates the pressure distribution induced on the target surface, which is then used as the input in the ABAQUS FE simulation to find the stress and deformation at the laser peened site. However, before applying the model, it was first studied in greater detail to investigate the functionality of the model.

Model Overview and Theory

The multi-physics numerical analysis is based on the two-dimensional axisymmetric hydrodynamic governing equations, which include; conservation of mass, momentum, and energy for the confinement (water) and coating (Al) layers. These equations are split into matrices, equations 1-4, in which they will be differentiated with respect to time, radial direction, r, depth, z, or simply a function of r, respectively (equation 5).

$$H_t = \begin{bmatrix} \rho_C \\ \rho_{CL} \\ \rho u \\ \rho v \\ E_i + KE \end{bmatrix} \tag{1}$$

$$H_r = \begin{bmatrix} \rho_C u \\ \rho_{CL} u \\ \rho u^2 + P \\ \rho uv \\ [E_i + KE + P]u + q_r + Q_r \end{bmatrix} \tag{2}$$

$$H_z = \begin{bmatrix} \rho_C v \\ \rho_{CL} v \\ \rho u v \\ \rho v^2 + P \\ [E_i + KE + P]v - I + q_z + Q_z \end{bmatrix} \tag{3}$$

$$H = \begin{bmatrix} \rho_C u \\ \rho_{CL} u \\ \rho u^2 \\ \rho u v \\ [E_i + KE + P]u + q_r + Q_r \end{bmatrix} \tag{4}$$

$$\frac{\partial}{\partial t}(H_t) + \frac{\partial}{\partial r}(H_r) + \frac{\partial}{\partial z}(H_z) + \frac{1}{r}(H) = 0 \tag{5}$$

, where ρ_c and ρ_{CL} are the densities of the coating, aluminum in this study, and the confinement layer (water), respectively, ρ is the total density, $\rho = \rho_c + \rho_{CL}$, P the pressure, E_i the volumetric internal energy, T the temperature, and is I the net flux in laser radiation. KE is the kinetic energy, where $KE = \rho(u^2 + v^2)/2$, q_r and q_z are the thermal conduction heat fluxes in the r- and z-directions, and Q_r and Q_z are the radiation [41] in the r- and z-directions, respectively. These can be found using the radiative transfer equation in the diffusion approximation and the Planck technique to average the absorption coefficient, k_v. Equation 6-9 shows the approximation for the z-direction.

$$\frac{\partial Q_v}{\partial z} + ck_v U_v = ck_v U_{bv} \tag{6}$$

$$Q_v = -\frac{c}{3k_v}\frac{\partial U_v}{\partial z} \tag{7}$$

$$U_{bv} = \frac{8\pi h v^3}{c^3 e^{\left(\frac{hv}{kT}\right)} - 1} \tag{8}$$

$$Q_z = \int Q_v dv \tag{9}$$

, where U_v is the spectral energy density of radiation, U_{bv} is the blackbody radiation, v is the radiation frequency, c is the speed of light, k is the thermal conductivity, and h is Planck's constant.

The thermal conduction heat fluxes, q_r and q_z, are found using equations 10 and 11, respectively.

$$q_r = -k\frac{dT}{dr} \tag{10}$$

$$q_z = -k\frac{dT}{dz} \tag{11}$$

Using density and temperature tables the model determines whether the material at a given time and point in space is water (confinement medium), aluminum (ablative coating), or plasma, which is considered a mixture of water and aluminum. If aluminum, it deploys the quotidian equation of state (QEOS). If plasma, the same QEOS model used for aluminum is deployed, which includes Lee & More's [42] model for thermal and electrical conductivities for dense plasmas. If water, the model uses Ree's equation of state (EOS) for water [47]. A self-closed thermal model presented in Ref. [19] can be used to find the physical properties such as receding velocity of the coating and expansion of the water. For all states, Drude theory is used to find the absorption coefficient, index of refraction, and reflectivity.

For the aluminum and plasma, Lee and More model is used in conjunction with the Boltzmann equation to find the transport properties, such as thermal and electrical conductivities, k and σ_0, respectively [1]. In equations 12-16, n_e is the electron density, m is the electron mass, k_B is the Boltzmann constant, T is temperature, and μ is the chemical

potential. A^α and A^β can be solved using Fermi-Dirac integrals, as shown in equations 14-16, which are functions of μ/k_bT [2].

$$k = \frac{n_e k_B (k_B T)\tau}{m} A^\beta \left(\frac{\mu}{k_B T}\right) \tag{12}$$

$$\sigma_e = \frac{n_e e^2 \tau}{m} A^\alpha \left(\frac{\mu}{k_B T}\right) \tag{13}$$

$$A^\alpha \left(\frac{\mu}{k_B T}\right) = \frac{4F_3}{3[1 + e^{\left(-\frac{\mu}{k_B T}\right)}]F_{1/2}^2} \tag{14}$$

$$A^\beta \left(\frac{\mu}{k_B T}\right) = \frac{20F_4 [1 - \frac{16F_3^2}{15F_4 F_2}]}{9[1 + e^{\left(-\frac{\mu}{k_B T}\right)}]F_{1/2}^2} \tag{15}$$

$$F_j \left(\frac{\mu}{k_B T}\right) = \int_0^\infty \frac{t^j}{1 + e^{(t - \frac{\mu}{k_B T})}} dt \tag{16}$$

Next, the index of refraction and absorption coefficients of aluminum can be found using the Drude theory, as given in equations 17-21, where w_p is the plasma frequency, v is the collision frequency, σ_0 is the DC electric conductivity, ε_0 is the permittivity of vacuum, n_e is the electron number density, m' is the mass of electrons, w is the laser frequency, c is the speed of light, and α is the absorption coefficient. n_r and n_i are the real and imaginary parts of the complex index of refraction [2] [3].

$$v = \frac{n_e e^2}{m' \sigma_0} \tag{17}$$

$$w_p = \sqrt{\frac{n_e e^2}{m' \varepsilon_0}} \tag{18}$$

$$n_r^2 - n_i^2 = 1 - \frac{w_p^2}{w^2 + v^2} \tag{19}$$

$$2n_r n_i = \frac{v w_p^2}{w(w^2 + v^2)} \tag{20}$$

$$\alpha = \frac{2w n_i}{c} \tag{21}$$

For the water confinement region, the QEOS model used for the aluminum layer was found to be very approximate for the water layer and therefore was not used. Instead, Ree's EOS model from Ref. [43] was used and includes temperatures ranging from room temperature up to 25 keV and densities from 2 g/m^3 to 400 Mg/m^3 from theoretical and experimental studies. It considers the ionization process and chemical equilibrium from the dissociation products of the water. The index of refraction and absorption coefficient for the water to plasma region are calculated from the Drude model shown in equations 22-27.

$$\varepsilon' = 1 - \frac{w_p^2}{w^2 + \gamma^2} \tag{22}$$

$$\varepsilon'' = \frac{\gamma w_p^2}{w(w^2 + \gamma^2)} \tag{23}$$

$$w_p = \sqrt{\frac{n_e e^2}{m \varepsilon_o}} \tag{24}$$

$$\gamma = n_p \sigma_c \sqrt{\frac{8 k_B T_e}{\pi m}} \tag{25}$$

$$n_{prf} = \sqrt{\frac{\varepsilon' + \sqrt{\varepsilon'^2 + \varepsilon''^2}}{2}} \tag{26}$$

$$k_{prf} = \frac{\varepsilon''}{2n_{prf}} \tag{27}$$

, where ε' is the real part and ε'' is the imaginary part of the dielectric function of plasma, respectively. The laser frequency is w, k_B is Boltzmann's constant, T_e is the electron temperature, ε_o is the dielectric constant of vauum, e is the electron charge, and w_p is the plasma frequency. n_{prf} and k_{prf} are the real and imaginary parts of the refractive index of plasma, respectively, and n_{wrf} and k_{wrf} are the real and imaginary parts of index of refraction of water (unshocked: $n_{wrf} = 1.33$, $k_{wrf} = 0$). [4]

Using the index of refraction values, the water-plasma interface reflectivity to laser radiation, R_{wp}, and can be calculated using:

$$R_{wp} = \frac{(n_{prf} - n_{wrf})^2 + (k_{prf} - k_{wrf}^2)}{(n_{prf} + n_{wrf})^2 + (k_{prf} + k_{wrf})^2} \tag{28}$$

Then the absorbed power density of the laser can be computed using the initial laser power density, absorption coefficient, and index refraction at each point in space.

Next, the thermodynamic functions of pressure and energy are calculated using Helmholtz free energy, shown in equations 29-37. In equation 29, F_e and F_i are the semi-classical electron free energy, and ion free energy, respectively. F_b is a semi-empirical correction factor is included for the bonding effects in the solid state. This correction factor allows for an approximately correct equation of state for the aluminum region, which has been experimentally tested to verify [44]. From equations 30-37, the pressure (P), entropy (S), and energy (E) can be obtained, based on free energy. Similar to free energy, pressure, entropy, and energy also have the ion, semi-classical electron, and semi-empirical

correction parts as well, denoted by subscripts i, e, and b, respectively. The total pressure and energy can be calculated using equations 36 and 37, respectively.

$$F = F_e + F_b + F_i \tag{29}$$

$$P_b = \rho^2 \frac{\partial F_b}{\partial \rho} \tag{30}$$

$$S_b = -\frac{\partial F_b}{\partial T_e} \tag{31}$$

$$E_b = F_b + T_e S_b \tag{32}$$

$$P_i = \rho^2 \frac{\partial F_i}{\partial \rho} \tag{33}$$

$$S_i = -\frac{\partial F_i}{\partial T_i} \tag{34}$$

$$E_i = F_i + T_i S_e \tag{35}$$

$$P = P_e + P_i + P_b \tag{36}$$

$$E = E_e + E_i + E_b \tag{37}$$

The Cowan model is used for the ion portion and combines the ideal gas law, fluid scaling law, Lindemann melting law, Dulong-Petit law, Gruneisen pressure law, Debye lattice theory, and Nernst theorem (3rd Law of Thermodynamics) to form a single analytical model [4]. The model is divided into two largely independent parts, the "structural part" and phenomenological part". The "structural part" is based on expressions for melting temperature, $T_m(\rho)$, and Debye temperature, $\Theta_D(\rho)$, and the "phenomenological part"

predits $T_m(\rho)$ and $\Theta_D(\rho)$ for any material [4]. Equations 38 and 39 give scaling variables, u and w, for the "structural part" of the model. [4, 2]

$$u = \frac{\Theta_D(\rho)}{T} \tag{38}$$

$$w = \frac{T_m(\rho)}{T} \tag{39}$$

By the Lindemann melting law,

$$\frac{w}{u^2} = \frac{\alpha T}{\rho^{2/3}} \tag{40}$$

The ion free energy equation (equation 41) depends on the phase of the material, solid or fluid phase. Solid phase (i.e. aluminum) corresponds to $w > 1$ and fluid phase (i.e. water) corresponds to $w < 1$. Where k_B is the Boltzmann's constant, m_p is the mass per atom, and T is temperature. [4, 2]

$$F_i(\rho, T) = \left(\frac{k_b T}{m_p}\right) f(u, w) \tag{41}$$

For the low temperature solid phase, $f(u,w)$ is described in equation 42, where $w>1$ and $u>3$ [4].

$$f = \frac{9u}{8} + 3\log(1-e^{-u}) - \frac{\pi^4}{5u^3} + e^{-u}\left(3 + \frac{9}{u} + \frac{18}{u^2} + \frac{18}{u^3}\right) \tag{42}$$

For high-temperature solids, $f(u,w)$ is described in equation 43, where $w > 1$ and $u < 3$. [4]

$$f = -1 + 3 \log u + \left(\frac{3u^2}{40} + \frac{u^4}{2240}\right) \tag{43}$$

For the fluid phase, where $w<1$, $f(u,w)$ is described in equation 44. [4]

$$f = -\frac{11}{2} + \frac{3}{2} \log\left(\frac{u^2}{w}\right) + \frac{9u^{1/3}}{2} \tag{44}$$

Next, a modified Thomas-Fermi statistical [4] model is used to find the electronic properties. The electrons are modeled as charged fluid surrounding the nucleus and finite temperature Fermi-Dirac statistics are used to find the properties of the electron gas. Each nucleus is at the center of a spherical cavity, as given in equation 45 [2].

$$R_o = \left(\frac{3\pi n_i}{4}\right)^{1/3} \tag{45}$$

, where R_o is the cavity radius and n_i is the total ion number density.

Then the Poisson equation is used to find the electrostatic potential, $V(r)$, within the ion sphere.

$$\nabla^2 V(r) = 4\pi e n(r) - 4\pi Z e \delta(r) \tag{46}$$

, where e is the electron charge, Z is the atomic number, μ is the electron chemical potential, and $n(r)$ is the total electron number density. The total electron number is given in equation 47 and includes both bound and free electrons. c_1 and $F_{1/2}$ can be calculated using equations 48 and 49. The electron chemical potential, μ, can be found using equation 50, which is the requirement that the cell must be neutral. Then $V(r)$, μ, and $n(r)$ can be obtained by solving equations 46-50 simultaneously [2].

$$n(r) = c_1(k_bT)^{3/2}F_{1/2}\left[-\frac{\mu + eV(r)}{k_bT}\right] \tag{47}$$

$$c_1 = (\frac{\pi^2}{2})(\frac{2m}{h})^{3/2} \tag{48}$$

$$F_j(y) = \int_0^\infty \frac{x^j dx}{1 + e^{(x+y)}} \tag{49}$$

$$\int n(r)dV_{ol} = Z \tag{50}$$

Finally, the remaining components of the thermodynamic energy and pressure, the electron parts, can be calculated using equations 51-55, below [2].

$$K = c_1(k_BT)^{5/2} \int F_{3/2}[-\frac{\mu + eV(r)}{k_BT}]dV_{ol} \tag{51}$$

$$U_{en} = -\int \frac{Ze^2n(r)}{|r|}dV_{ol} \tag{52}$$

$$U_{ee} = \frac{e^2}{2}\int\int[-\frac{n(r')n(r)}{|r-r'|}dV_{ol}\,dV_{ol}' \tag{53}$$

$$E_e = (K + U_{en} + U_{ee})/m_p \tag{54}$$

$$P_e = \frac{2}{3}c_1(k_BT)^{5/2}F_{3/2}(-\frac{\mu}{k_BT}) \tag{55}$$

Model Setup and Simulation Conditions

Using the theory described in the previous section and an essentially non-oscillatory (ENO) finite difference scheme, the hydrodynamic governing equations are solved at each time step and position in space. ENO schemes are usually used to solve advection cases,

making it very effective for simulating shock wave produced during laser peening [45]. An overview of the model is shown in the flow chart, below (Figure 2).
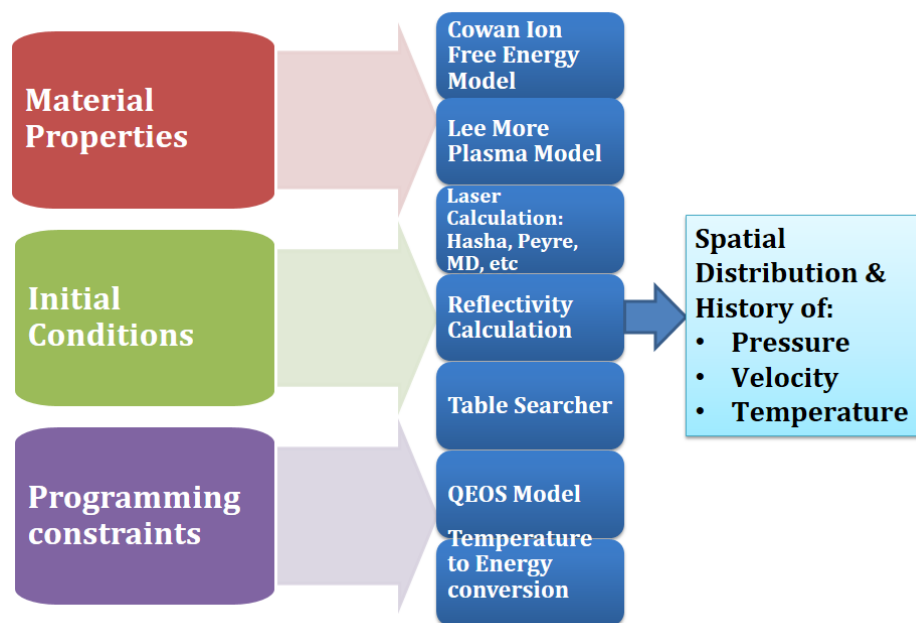

Figure 2. Flow chart for the physics based model of laser-induced high pressure plasmas.

First, the tables of temperature and density for the confinement layer and coating material are ordered from low to high. Next, the simulation domain is defined, including; domain size, mesh, simulation time, time step, and the confinement layer thickness and absorption coefficient. The user can then define cross-sections and times at which the pressure, temperature, energy, etc. should be output.

The model then reads the initial conditions and does another check to make sure the tables are in order from low to high. Now, the hydrodynamic governing equations, equations 1-4, are defined as matrices and the conduction term is included everywhere except for the edges of the domain. First, the energy is calculated using the temperature and pressure from the EOS models. The model determines the material based on density,

and the appropriate EOS is called. If density does not fit the criteria for water or aluminum, it is assumed to be plasma, a mixture of water and aluminum particles, and the corresponding equations are called.

Next, the transport properties are calculated, which is based on the state (liquid/solid/plasma) during any given time during the simulation. The model determines what state a given point in the domain is in based on the density at a given point in the domain. Also, if the temperature is above 11600 K, the material is assumed to be plasma and corresponding equations are used.

As the model begins to solve, it starts stepping through the time increments, calculating the power density based on the laser parameters defined in the laser calculation file. For optimal use of the model, it was determined that the time increments, dt, should be set to $0.0001 \times \Delta z$, the grid step in the z-direction. In this study the time increments are 0.01 ns and the total simulation time is set to be 20 ns. These parameters should be defined by the user before starting the simulation. Parameters to be defined include pulse duration, power density, laser spot size, and the spatial and pulse distributions of the power density of the laser. Some options for these spatial and pulse distributions of laser power density are shown in Figure 3 and Figure 4. Using laser parameters and the previously described physics models, the discretized governing equations are solved at each time step and point in space for the temperature, pressure, energy, velocity, etc. The domain and mesh generation for the analysis is described in the next section.
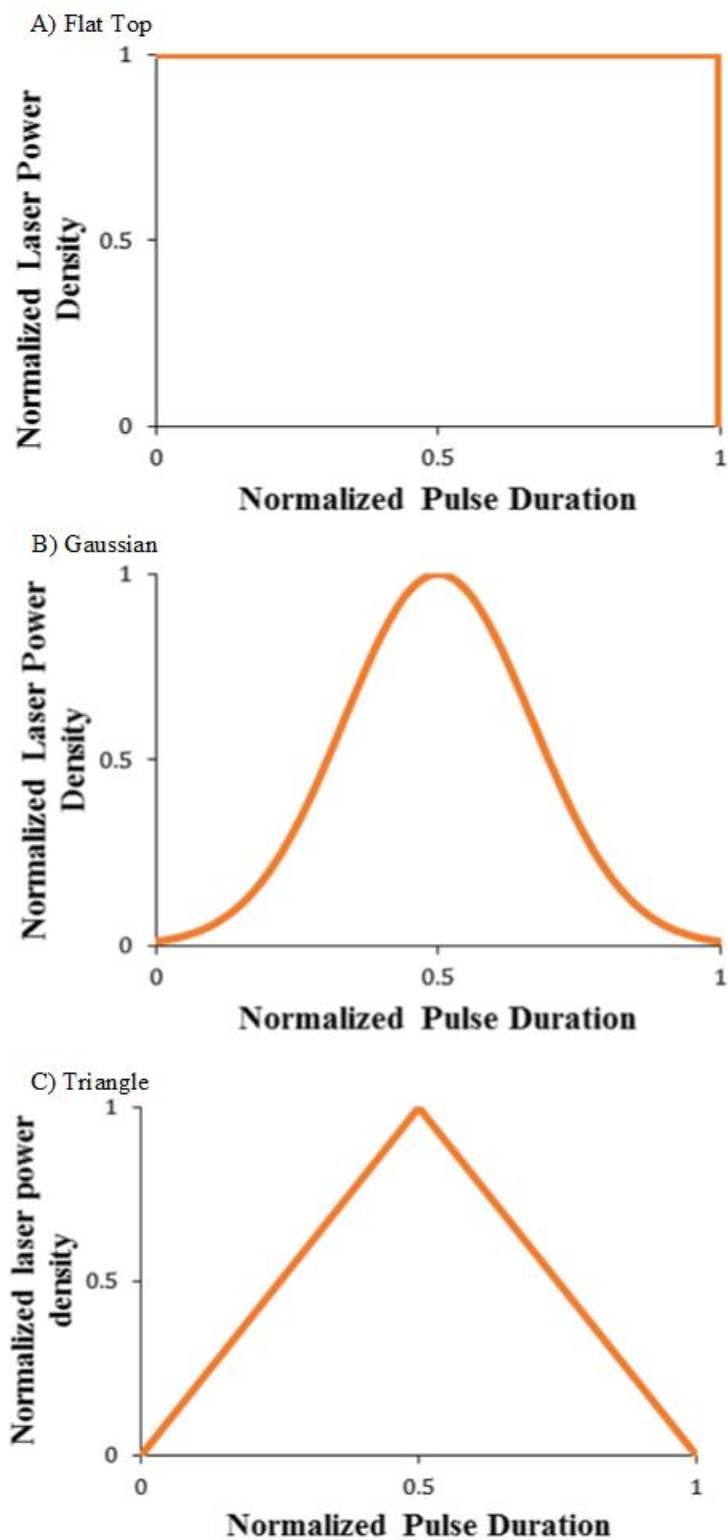
Figure 3. Normalized laser profiles (time). A: Flat Top, B: Gaussian, and C: Triangle.
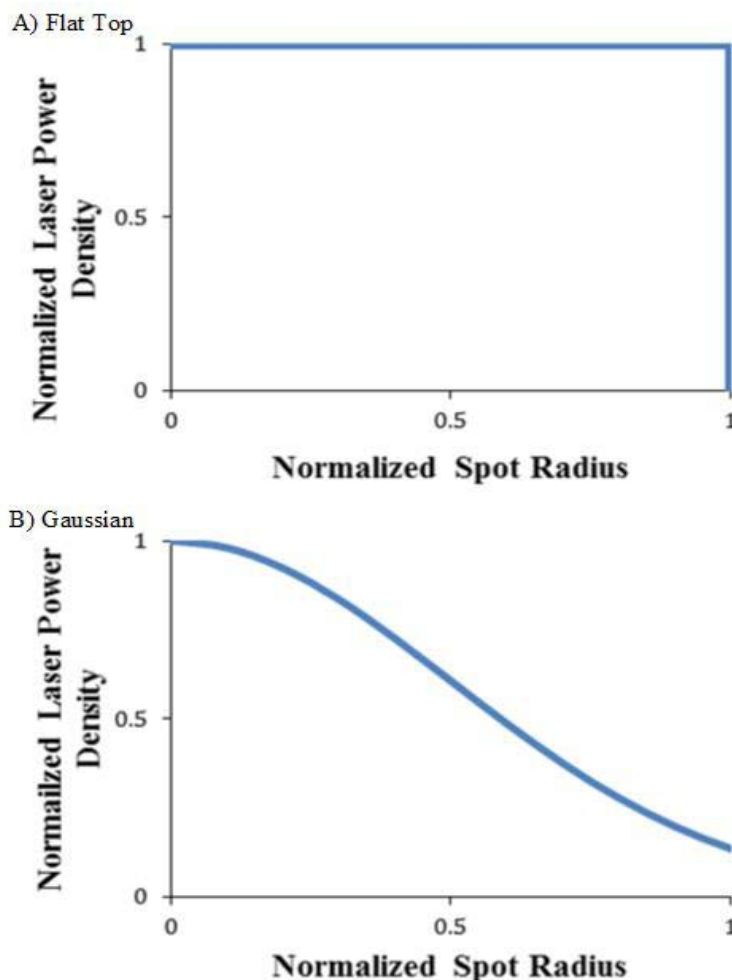
Figure 4. Normalized laser space shapes, where the center of the laser spot is at 0. A: Flat and B: Gaussian.

Domain and Mesh Generation

A schematic of the model setup is shown in Figure 5, where the spatial distribution is assumed to be symmetric in the radial direction, therefore the process is considered axisymmetric about the r-axis. For the radial direction, the domain size is 3 mm, with 800 nodes for the mesh. For the z-direction the domain size is 60 μm, with a fine mesh around the coating-water interface, where the plasma will be generated and the high pressures will be induced, and a coarse mesh above and below this region. The simulation domain and mesh can be seen in Figure 6 and how this region correlates to an actual laser peening setup

is shown in Figure 5. The confinement layer-coating interface is located at $z = L_z/2$, or $z = 30$ μm for this analysis, where the water is at $z > 30$ μm, and the coating is at $z < 30$ μm. Laser radiation transmitted through the breakdown plasma is directed in the z-direction and is symmetric about the $r = L_r/2 = 0$. The model only simulates from $L_r/2$ and to the right, since this process is assumed to be axisymmetric.
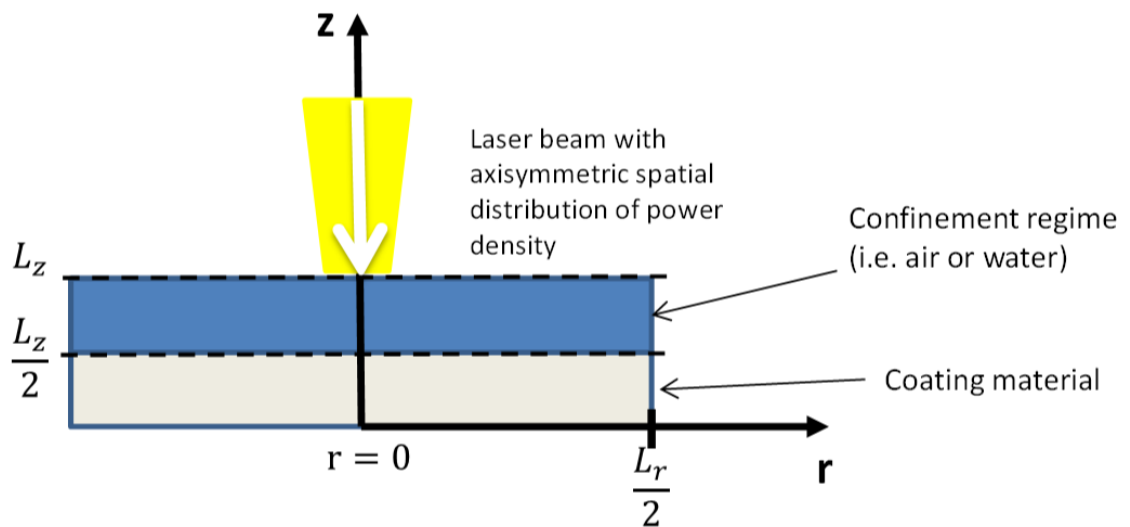
Figure 5. Model setup schematic.
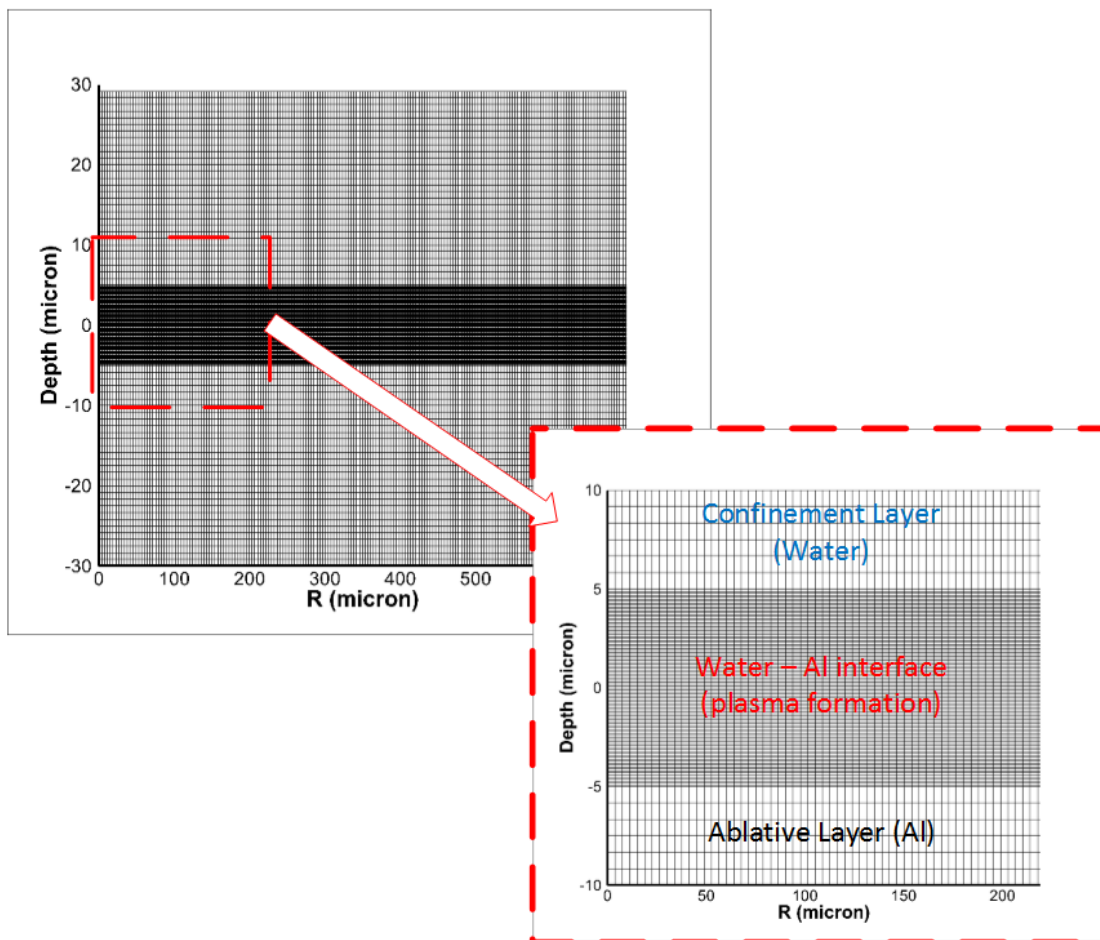
Figure 6. Mesh for numerical modeling with the fine mesh section, near coating-water interface, in the red dashed box.

Simulation Results

First, simulations were conducted to compare with the results from Wu & Shin [4], and also with the experimental results from Peyre et al. [46] to verify the functionality of the model. An analyses of varying laser spot sizes was conducted and the spatial distribution of pressures at the coating surface were calculated. The results were normalized and plotted in the radial direction at time = 2.5 ns in Figure 7. When plotting the various spot sizes together, it can be seen that when r_o = 300 micron, the spatial distribution of the pressure has approximately the same profile as the top flat laser beam profile that was used for the simulation. As seen in Figure 7, as r_o decreases, the pressure

distribution deviates away from this flat top profile, this is consistent with the results of Wu & Shin [4]. As seen in the comparisons between experimental results [46] and model predictions in Figure 8, the model predicts the peak pressure on the target surface accurately, both showing a linear relationship between power density and peak pressure.
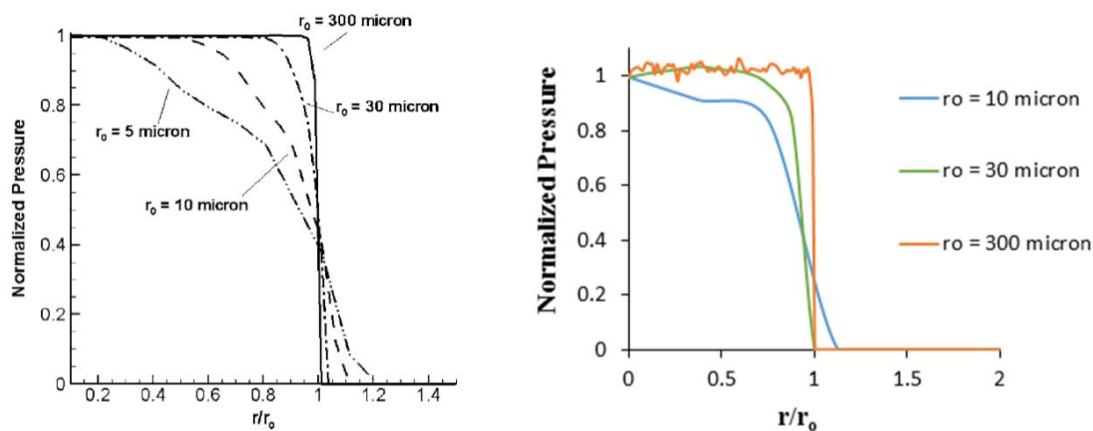
Figure 7. Normalized spatial distribution of pressures induced on the coating surface in the radial direction for various laser spot sizes, r_o, with a power density of 4 GW/cm^2. Results from Wu & Shin [4] on the left.
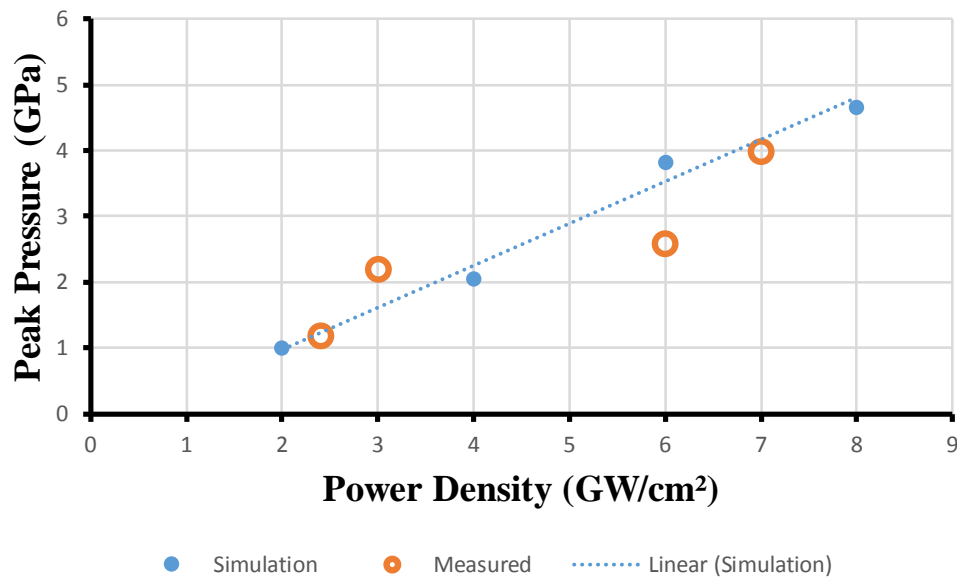
Figure 8. Comparison of model predicted and measured peak pressures for varying power density at the ablative coating surface using a laser with a 3 ns pulse duration and 1064 nm wavelength [46].

Next, the effect of power density distribution over the pulse duration on the history of the pressure induced over the simulation time was analyzed to determine which option should be used for accurate modeling. Some of these options are shown in Figure 3, in which the flat top distribution in the simplest, supplying a constant power density over the entire pulse duration. The triangle and Gaussian become slightly more computationally expensive and more complex to implement, both in the physic-based modeling and when using a finite element software when inputting the predicted pressure distributions.
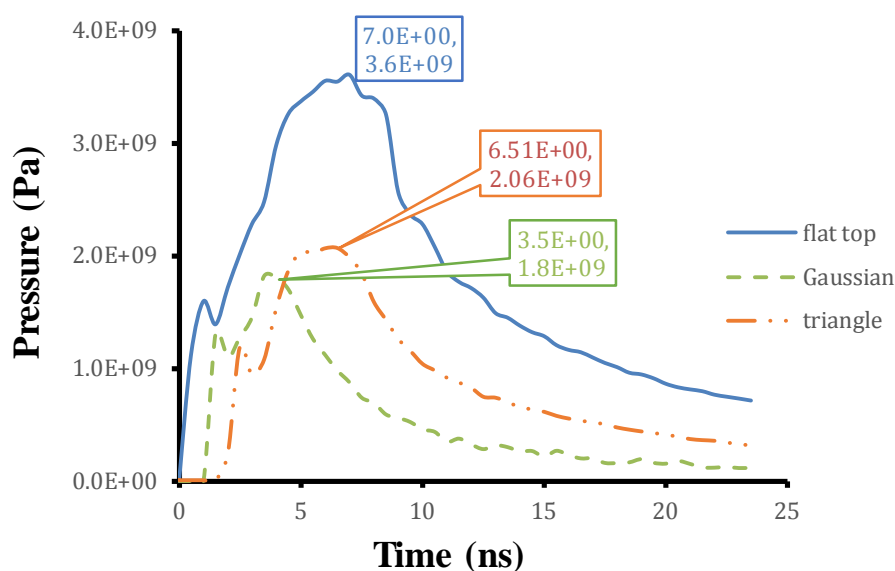
Figure 9. Pressure histories comparing flat, Gaussian, and triangular laser profiles (t).

Similarly, the effect of the laser space shape was taken into consideration, a simple flat-top and Gaussian laser space shapes were simulated, and shown in Figure 10 and Figure 11. The flat-top simulates a constant laser pulse energy over the entire beam radius and is less computationally expensive than producing a Gaussian space shape, which models the laser pulse energy in a Gaussian shape over the beam radius, as shown in Figure 4. Both simulations were conducted for a beam radius of 300 μm, however the Gaussan simulation only shows significantly higher pressures out to 200 μm, whereas the flat-top has significant induced pressures over the entire beam radius. The obviously differences in pressure distributions at the coating-water interface, as seen in Figure 10 and Figure 11, mean the Gaussian distribution for the space shape should be used for accurate predictions.
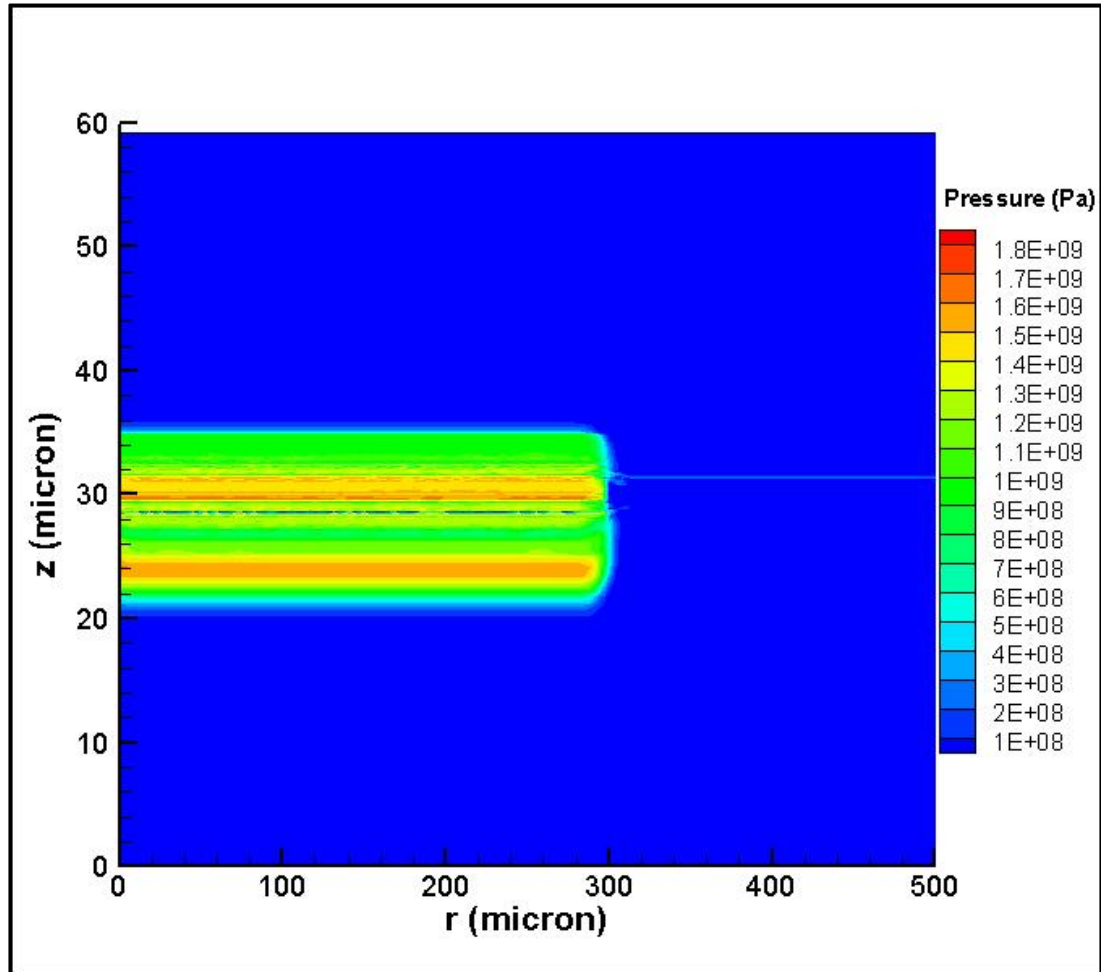
Figure 10. Pressure distribution at t = 4 ns for a flat-top laser space shape (r) with beam radius: 300 μm, power density: 4 GW/cm^2, and pulse duration: 8 ns.
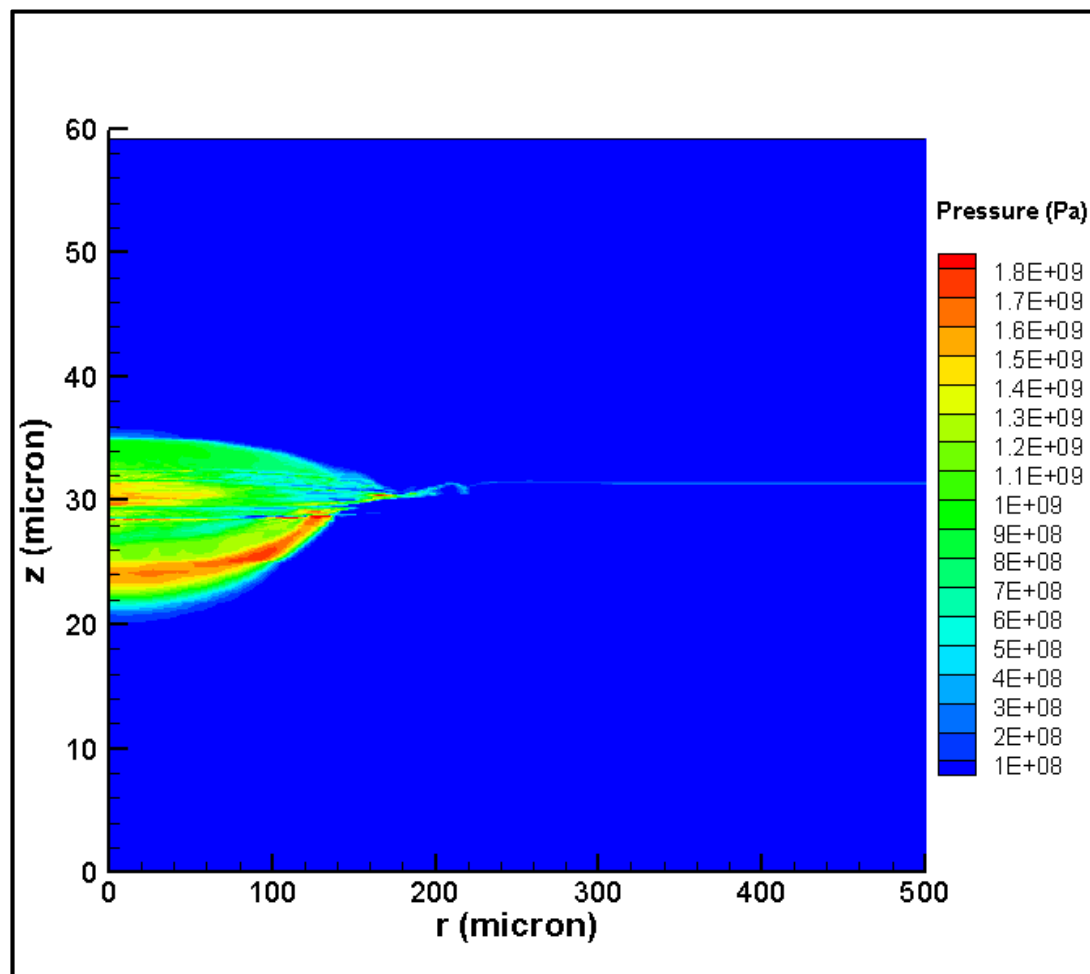
Figure 11. Pressure distribution at t = 4 ns for a Gaussian laser space shape (r) with beam radius: 300 μm, power density: 4 GW/cm^2, and pulse duration: 8 ns.

After verifying the working condition of the model using previous publications, simulations were conducted using the laser parameters used for the experiments in the following chapters. The parameters are shown in Table 1, where the beam diameter was 1.24 mm, power density 3.2 GW/cm^2, and pulse duration was 8 ns. The triangular laser profile (with respect to time) and Gaussian space shape, shown in Figure 3 and Figure 4, respectively, were used for the peening simulations.

Table 1. Laser parameters for simulation results

Laser pulse energy (mJ)	380
Beam Radius (mm)	0.62
Power Density (GW/cm^2)	3.2
Pulse Duration (ns)	8
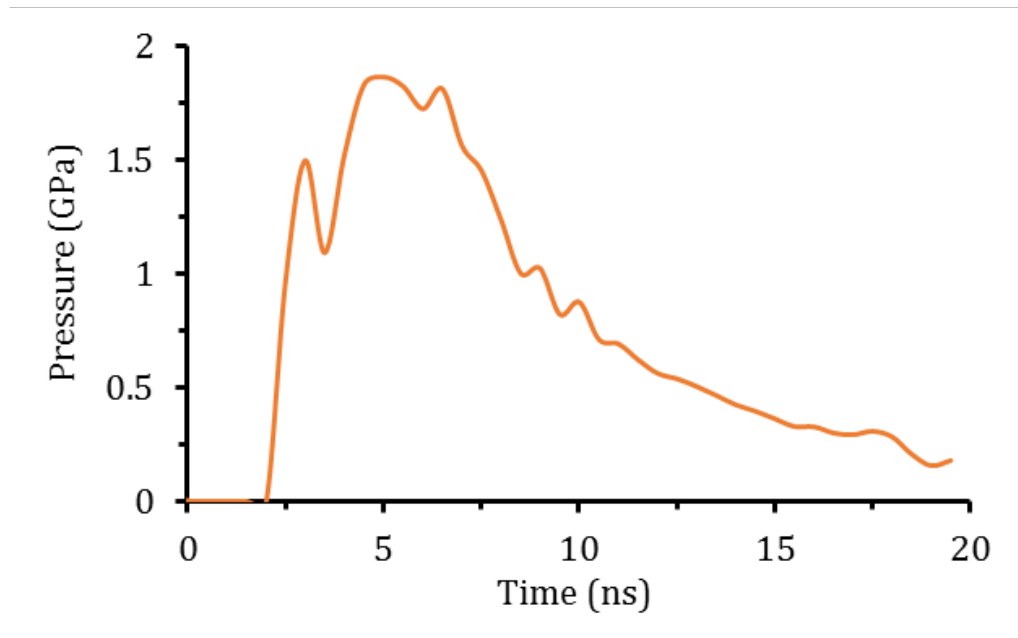
Figure 12. Pressure history near the coating-water interface (8 ns pulse duration, 3.2 GW/cm^2 power density).

From Figure 12 above, it can be seen that although the laser power intensity in terms of time is defined to follow a triangle shape (Figure 3), the pressure does not follow the same shape. While the peak intensity occurs at 4 ns, the peak pressure induced near the coating-water interface does not happen until roughly 5 ns, as seen in Figure 12. For this reason, the pressure distribution was plotted at 5 ns for the laser parameters listed in Table 1, to find the location at which this peak pressure occurs. The two-dimensional distribution in the radial and depth directions is shown in Figure 13, where the coating-water interface

is near the depth = 0 plane and the pressure distribution is considered axisymmetric about the R-axis.   The peak pressure is just below the coating-water interface and is about 2 GPa.
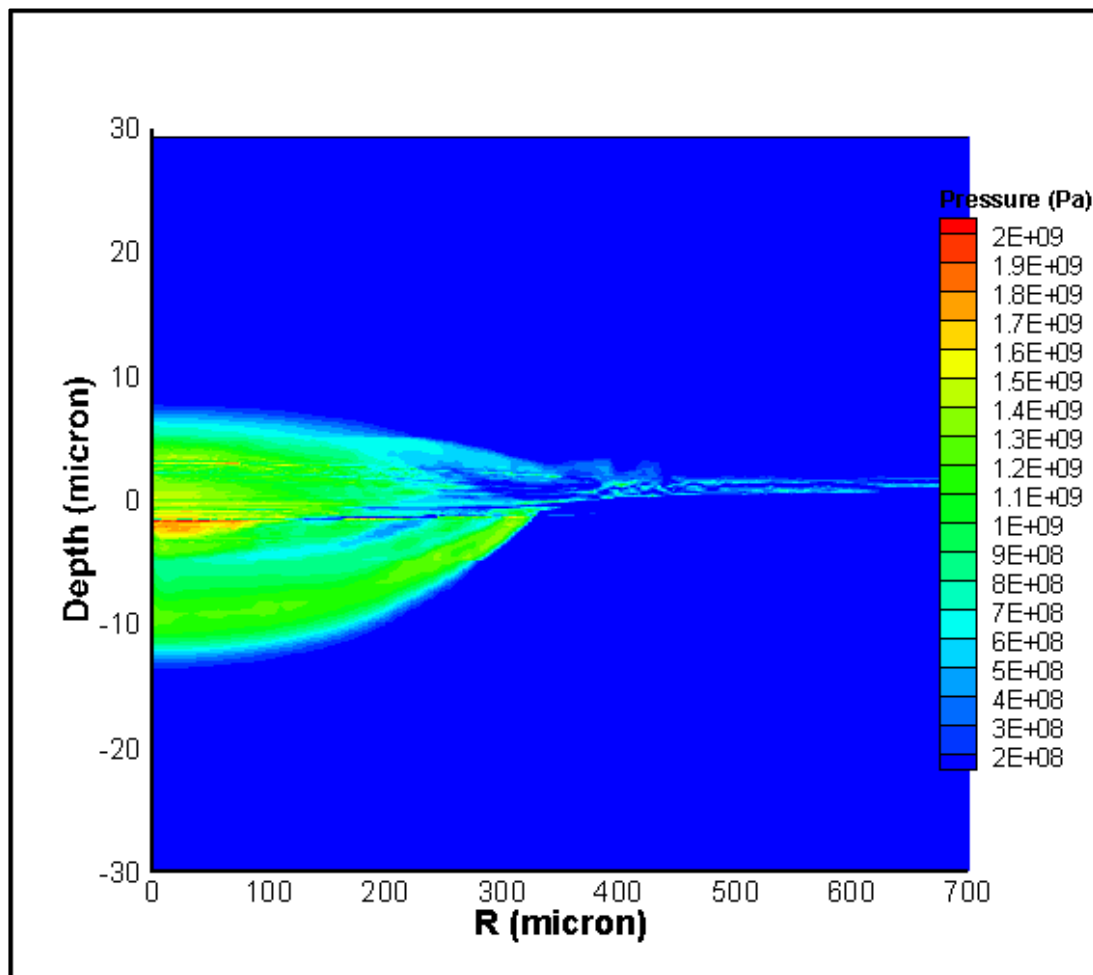
Figure 13. Pressure distribution at 5 ns for laser parameters listed in Table 1.

Conclusion

After comparing the results obtained in the simulations above with experimental results, as well as other published simulation results using this same technique, it was concluded that this multi-physics modeling technique can be used to accurately predict the induced pressure distribution on the surface of the laser peened target material.

Also, after obtaining the functions for the pressure induced on the surface in terms of time and space, the data was entered into ABAQUS for finite element analysis of the experiments conducted in Chapter IV, in which the deformation depth was very important for the application at hand. Later in this work it is shown that by using the model predicted pressure distribution as load inputs for ABAQUS simulations of the applications studied, accurate deformation predictions can be obtained, when compared to experimental results. This shows that the multi-physics based model discussed in this chapter seems to predict the induced pressures accurately.

CHAPTER IV

EXPERIMENTAL STUDY OF SHEET METAL MICRO-BENDING

Introduction

In this chapter, the application of sheet metal bending using the HEPLP process is investigated. In order to address the deformation control technique in laser micro-bending, various experiments are conducted on thin aluminum sheet in one-side shock configuration. The experiments are conducted using a nanosecond Nd:YAG pulse laser device. The bending angle evaluated in this research is less than 10°, which is usually the magnitude of deformation error for sheet metal generated in assembly processes. The technique presented in this study can be used to align the sheet to the desired dimensions. The effects of laser pulse energy, scanning scheme, and sheet thickness are examined and the bending mechanisms (positive and negative) are numerically analyzed using the multi-physics model from Chapter II coupled with a finite element (FE) model developed in ABAQUS [6].

Setup and Experiments

The setup for laser shock bending experiments conducted for this investigation is shown in Figure 14. The equipment are used in this study are described as follows. The laser used was a Q-switched Nd:YAG laser with a wavelength of 1064 nm, laser pulse repetition rate of 10 Hz and pulse duration of 7 ns. The laser pulse energy, E, was adjustable. The laser beam was directed at the target through a series of reflecting mirrors and a convergent lens with a focal length of 35 mm. With the use of the convergent lens, the laser beam was focused to a laser spot size, d, of 1.75 mm on the surface of specimen, as shown in Figure 14. The specimen was fixed at one end on a worktable in a water tank, which acted as the water-confinement regime. The depth of water-confinement layer was set to 10 mm from the surface of the specimen. The movement of specimen in x-and y-directions was controlled by two linear motion stages with a motion resolution of 0.01 mm.

Aluminum 1060 sheet metals were used as specimen material in this study. Each specimen was cut to 76 mm× 19 mm in size and had an initial bending angle less than 15'.
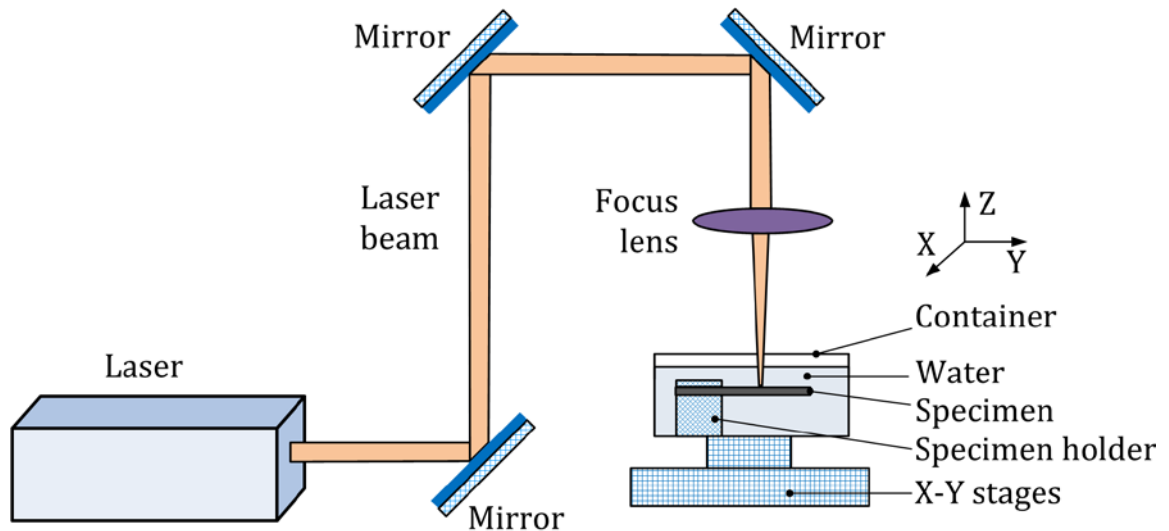
Figure 14. Experimental setup for sheet metal bending.

Before laser impact, the specimens were cleaned with acetone. Then the laser was scanned over the targeted surface area of the clamped specimen with use of the X–Y stage, in order to create a bulk, uniform bending of the large specimen. The laser scan path is shown in Figure 15, in which the laser starts from one free side of the specimen, then moves linearly across the specimen surface, moves over to the next position, and then reverses the track. The distance, P_x, between the two adjacent laser impacts and the overlapping area of the two laser pulses depends on the laser scan speed, V. The distance between the two laser scan lines, P_y, was set to 2 mm. The experimental conditions are given in Table 2. The specimen thickness was varied from 0.25 to 1.75 mm, laser pulse energy from 0.2 to 0.5 J, laser scan speed from 5 to 10 mm/s, and the number of laser scan tracks from 1 to 5 per test. The overlapping ratio of the adjacent laser impacts was dependent on the laser scan speed, and varied from 44 to 63 %.
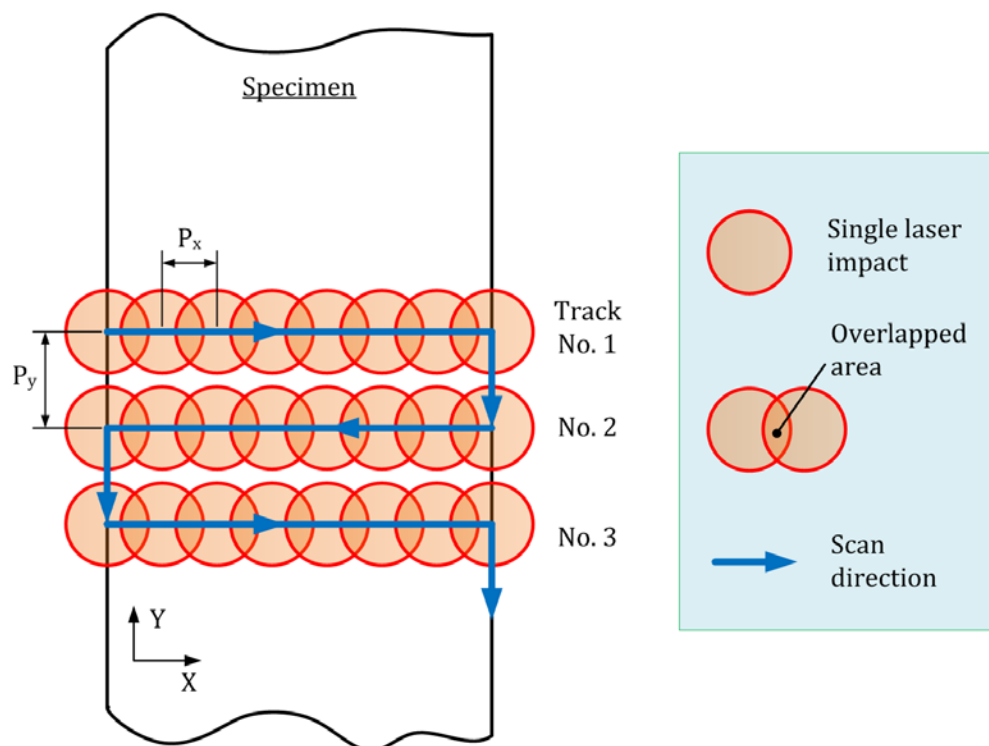
Figure 15. Laser scanning path.

Table 2. Experimental conditions

Parameters	Parameter range
Pulse energy, E (J)	0.2, 0.25, 0.3, 0.4, 0.5
Specimen thickness, t (mm)	0.25, 0.7, 0.88, 1.07, 1.75
Number of tracks, n	1, 2, 3, 5
Scanning speed, V (mm/s)	5, 7.5, 10
Overlapping ratio, OR (%)	44, 53, 63

A schematic of the specimen constraint and how the bending angle is measured after the experiment is shown in Figure 16. The profile of the bending angle was captured by a JGX-type 1 microscope and the edge lines of the image were detected by an image processing software. The bending angle could then be obtained by calculating the difference in the slopes of the two edge lines. The measurement had an accuracy of 1' per measurement. A positive bending angle was defined as bending towards the laser beam, while a negative bending angle is defined as bending away from the laser beam, as depicted in Figure 16. It should be noted that the bending angle evaluated in this study was less than 10°, which is usually the deformation problem of sheet metal generated in the assembly process [6].
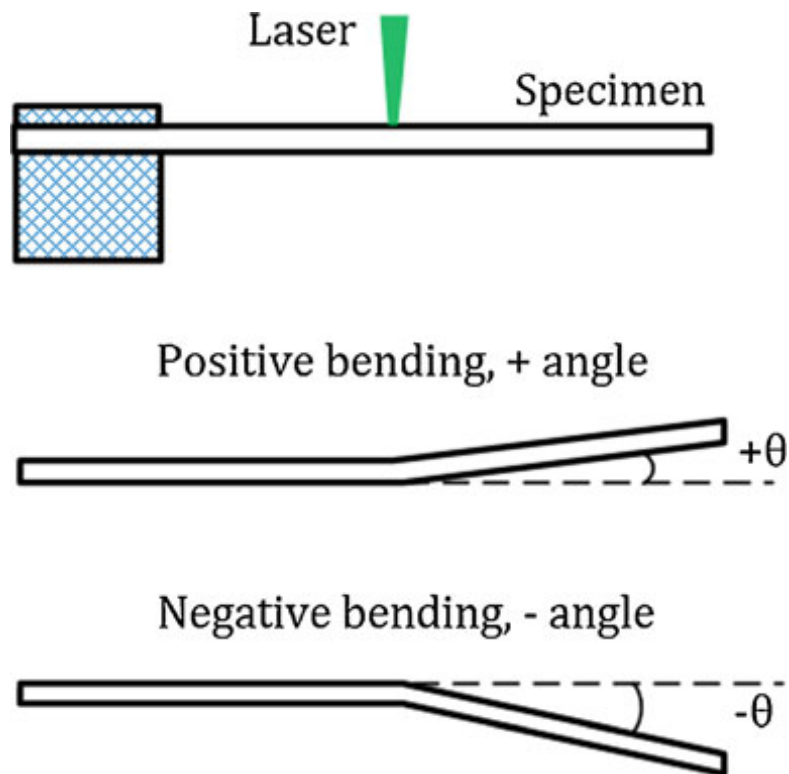
Figure 16. Bending angle measurement.

Experimental Results and Discussion

Table 3 shows the experimental results using the aforementioned technique of laser shock micro-bending, which are presented in my work in Ref. [6]. The positive–negative bending mechanisms were extensively investigated in Tests 1-16 for various specimen thicknesses and laser pulse energies. Specimen thicknesses of 0.7, 0.88, 1.07, and 1.75 mm, and four different laser pulse energies, 0.2, 0.3, 0.4, and 0.5 J (power density ranging from 1.2 to 3 GW/cm^2), were tested. Other process parameters such as laser spot size, overlapping ratio (or laser scan speed) and number of scan tracks were set constant. From these tests, both positive and negative bending angles were obtained. To ensure the repeatability of the experimental data, tests were conducted for each testing condition. Tests 17–25 were performed on 0.25 mm thick specimens in the positive bending domain. These tests investigated the effect of process parameters such as laser pulse energy, laser scan speed and number of scan tracks. As seen in Table 3, a three-level and three-factor design of experiments was implemented for nine different conditions. The laser pulse energy ranged from 0.2 to 0.3 J (or pulse power density of 1.2–1.8 GW/cm^2), overlapping ratio ranged from 44 to 63 % (or laser scan speed of 5–10 mm/s), and the number of scan tracks ranged from 1 to 3 [6].

Table 3. Experimental results

Test	t (mm)	I (GW/cm²)	E (J)	OR (%)	V (mm/s)	n	θ (')
1	0.70	1.2	0.20	63	5	5	65
2	0.88	1.2	0.20	63	5	5	-2
3	1.07	1.2	0.20	63	5	5	-9
4	1.75	1.2	0.20	63	5	5	-28
5	0.70	1.8	0.30	63	5	5	127
6	0.88	1.8	0.30	63	5	5	-1
7	1.07	1.8	0.30	63	5	5	-9
8	1.75	1.8	0.30	63	5	5	-28
9	0.70	2.4	0.40	63	5	5	130
10	0.88	2.4	0.40	63	5	5	22
11	1.07	2.4	0.40	63	5	5	-13
12	1.75	2.4	0.40	63	5	5	-29
13	0.70	3.0	0.50	63	5	5	133
14	0.88	3.0	0.50	63	5	5	27
15	1.07	3.0	0.50	63	5	5	-16
16	1.75	3.0	0.50	63	5	5	-31
17	0.25	1.2	0.20	44	10	1	18
18	0.25	1.2	0.20	53	7.5	2	118
19	0.25	1.2	0.20	63	5	3	176
20	0.25	1.5	0.25	44	10	2	146
21	0.25	1.5	0.25	53	7.5	3	396
22	0.25	1.5	0.25	63	5	1	132
23	0.25	1.8	0.30	44	10	3	310
24	0.25	1.8	0.30	53	7.5	1	102
25	0.25	1.8	0.30	63	5	2	376

Effect of Laser Energy on the Bending Mechanism

The bending angles with different laser pulse energies for different specimen thicknesses are shown in Figure 17. Positive bending was clearly observed in the specimen of 0.7 mm thickness, while negative bending appeared to be dominant for the thicker specimens (thicknesses of 1.07 and 1.75 mm). No apparent bending was observed for specimen of 0.88 mm thickness when the laser pulse energy was low (0.2–0.3 J); however, as the laser pulse energy increased to 0.4–0.5 J, a positive bending angle of about 27' was measured. For the thinner specimens (<0.88 mm), the laser energy is proportional to deformation, hence a higher laser energy corresponds with a larger positive bending angle. For instance, as the laser pulse energy increased from 0.2 to 0.5 J, the sheet bending angle increased from 65′ to 133′ for the specimens of 0.7 mm thickness.

For the negative bending angle, no significant effect can be found for laser pulse energy on the bending angle. This can also be seen in Figure 17. It appeared that the negative bending angle saturated at around −15′ and −30′ for 1.07- and 1.75-mm thick specimens, respectively [6].
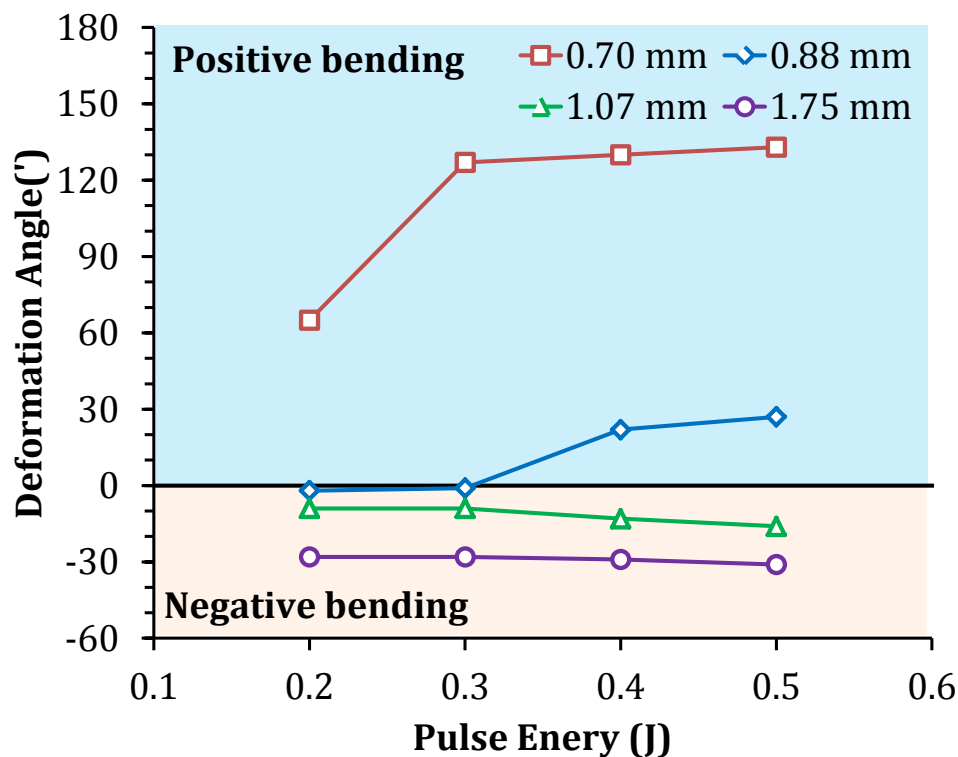
Figure 17. Relationship between energy and bending angle.

<u>Effect of Sheet Thickness on the Bending Mechanism</u>

Figure 18 examines the effect of specimen thickness on the bending mechanism. The specimen thickness is the apparent dominant factor in positive–negative bending transition, as the bending angle transitions from positive to negative as the specimen thickness increases. With thin specimens (0.7 mm), a positive bending angle was obtained for the laser pulse energy ranging from 0.2 to 0.5 J. When the specimen thickness increased to 1.07 mm or above, negative bending angle was obtained for all the laser pulse energies tested. The transition location was appeared to be located at a specimen thickness of 0.88 mm, in which the mechanism changes from positive to negative bending angle with increase in thickness beyond this point [6].
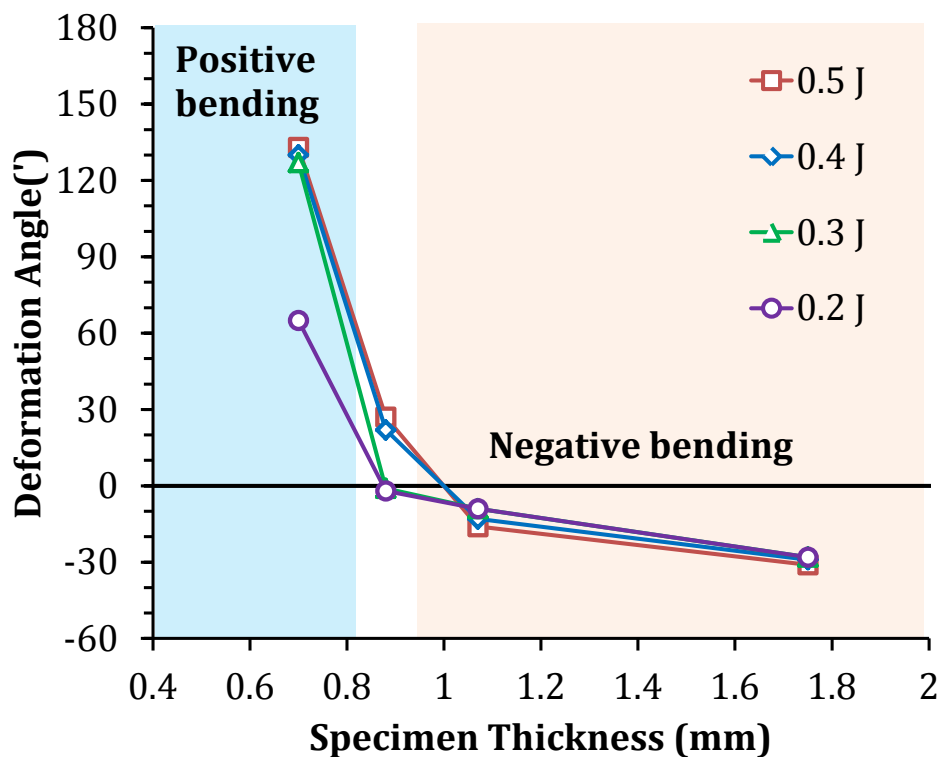
Figure 18. Relationship between sheet thickness and bending angle.

Modeling

To implement the laser bending technique in industry, it is crucial to be able to model and accurately control the bending angle of the sheet metal during the laser bending process. All of the laser parameters, scanning scheme, and work materials play critical roles in determining the bending angle. To numerically delineate the positive-to-negative bending mechanism, the laser shock micro-bending tests of 13 and 16 of two specimen thicknesses were simulated using a finite element model adopted from [2] with the commercial software ABAQUS 6.12-1. The workpiece domain is meshed using four-node thermally coupled axisymmetric quadrilateral, bilinear displacement, and temperature elements using reduced integration and enhanced hourglass control. Mechanical properties of Aluminum 1060 are shown in Table 4.

Table 4. Mechanical properties of Aluminum 1060

Property	Value
Density (kg/m^3)	2,672
Poisson's ratio, v	0.33
Elastic modulus (GPa)	72.4
Hugoniot elastic limit, HEL (GPa)	0.6

The laser-induced shock wave pressures were predicted using the multi-physics based hydrodynamic model discussed in Chapter III and applied as user-defined distributed time-dependent pressure loads in ABAQUS. The laser parameters used in these experiments produced a peak pressure above 3 GPa. To capture the dynamic nature of the shock wave in each laser shock peen impact, a fully coupled thermo-mechanical ABAQUS/Explicit analysis was first carried out for a time step of 2,000 ns. The resultant solution was then imported into the following implicit step, which then calculated the steady-state deformation using the ABAQUS/Standard solver. This method was used to save computation cost.

The simulation results of laser shock bending deformation are shown in Figure 19. Under the same laser energy loading conditions, the ratio l declines significantly as the specimen thickness increases from 0.7 to 1.75 mm, and the laser bending mechanism changes from positive to negative. It can be seen in Figure 19 that the predictions of the bending angles and deformation are very close to the measurements at various specimen thicknesses.
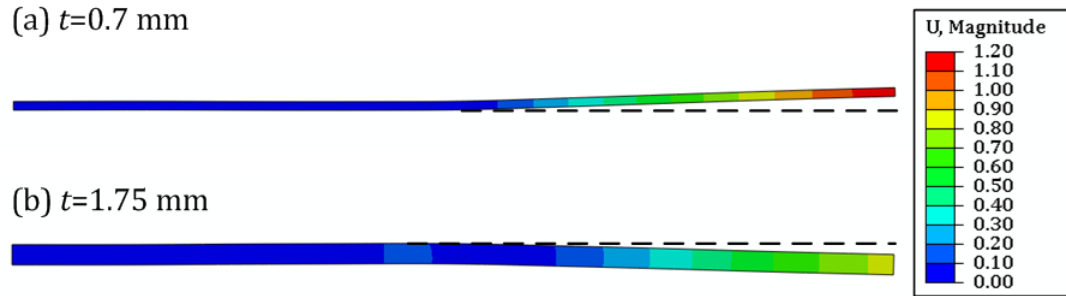
Figure 19. FEA results showing displacement U for sheet metal with thickness (a) 0.7 mm and (b) 1.75 mm.

From the results shown in Figure 18, it is obvious that the thickness is the dominant factor in determining the bending mechanism and it is approximated that the transition from positive to negative bending occurs at a thickness of about 0.88 mm. However, this transition thickness can be more accurately predicted using the relationship between specimen thickness and depth of plastic deformation. This theory is described as follows. During the laser shock bending process, plastic deformation occurs to a depth where the laser-induced shock wave pressure no longer exceeds the metal's Hugoniot elastic limit (HEL). The HEL of the target metal is related to the dynamic yield strength by [47]:

$$HEL = (\frac{1 - v}{1 - 2v})\sigma_Y^{DYN} \tag{56}$$

, where v is Poisson's ratio and σ_y^{dyn} is the dynamic yield strength at high strain rates. The HEL of the work material Aluminum 1060 was evaluated to be 0.6 GPa [48]. When the laser-induced shock wave peak pressure is less than the material HEL, no plastic deformation occurs and no residual stress is induced either. As the shock wave pressure is above 1 HEL, plastic deformation and plastic strain increase further and reach deeper into the target material. Therefore, the ratio of depth of laser pulse-induced plastic deformation and the specimen thickness, l, is determined by the laser induced shock wave pressure,

shock wave duration, work material properties and work material thickness, etc. Under the same laser parameters, the increase of specimen thickness decreases the ratio l, and vice versa. The laser positive-to-negative bending mechanism can be illustrated using the ratio l as shown in Figure 20. As the ratio l equals unity, i.e., the specimen is thoroughly strained, positive bending angle forms. As the ratio l is significantly less than unity, negative bending takes place [6].

(a) Positive bending

(b) Negative bending
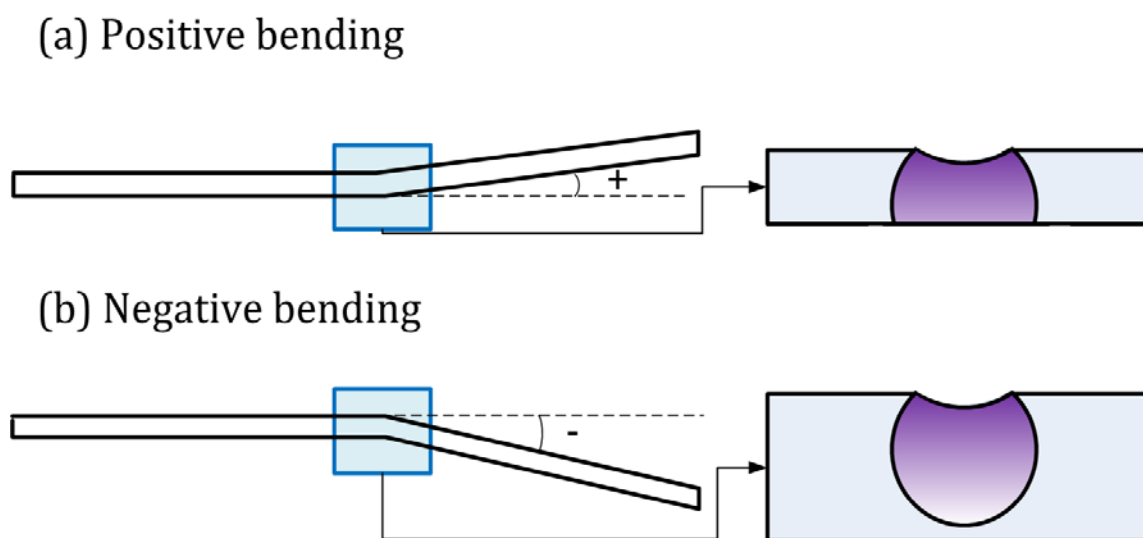
Figure 20. Deformation mechanisms in laser peen forming.

It is also desirable that a relationship be developed to determine the bending angle as a function of laser process parameters. Although bending angles appears saturated in the negative bending domain, positive bending angle is critically affected by the laser process parameters when the specimen thickness is thin. A multivariable regression analysis using the experimental data from Tests 1, 5, 9, 13, and 17–25 was conducted to establish a statistical model, which determines the sheet metal bending angle (θ, '). Four independent variables; sheet thickness (t, mm), laser pulse power intensity (I, GW/cm^2), overlapping ratio (OR), and passes of tracks (n) were selected as the four factors for this statistical

analysis. The obtained equation shows the predicted correlation between laser parameters and the sheet bending angle, which works well with estimation residuals less than 15 %.

$$\theta = 13.64I^{0.41}t^{-1.92}OR^{1.84}n^{1.16} \tag{57}$$

Note equation 57 only applies to positive bending for specimen thickness less than 0.7 mm. As can be seen in equation 57, specimen thickness plays an important role and has an adverse negative effect on the positive bending angle. The bending angle rises with the increase of overlapping ratio, passes of tracks, and laser pulse power intensity [6].

Conclusion

The specimen thickness and laser energy proved to the most prominent factors when determining the deformation of the laser micro-bending. The test results show that with the same laser parameters, thickness of the specimens is the most dominant factor in determining the deformation mechanism of the sheet. Comparing the thickest specimen of 1.75 mm and the thinnest specimen of 0.25 mm, it was clear that the deformation mechanism of the 0.25 mm thick sheet will be positive under all laser energy conditions, while the deformation mechanism of the 1.75 mm thick sheet will be negative under all laser energy conditions.

It was found that for the laser parameters used, laser energy only played an effect when the thickness of the sheet metal is below the transition thickness of about 0.88 mm. Then, with decreasing specimen thickness, the laser energy has more significant positive effects on the deformation of the sheet in the positive deformation mechanism conditions. For the negative bending mechanism, the bending angle shows very little change with the increase of the laser energy. It also appears that the negative bending angle saturates at a certain value, such as around $-15'$ and $-30'$ for 1.07 and 1.75 mm thick specimens, respectively.

As previously mentioned, a critical thickness threshold of 0.7–0.88 mm was found where the transition of positive–negative bending mechanism occurs. When the thickness is greater than the threshold, the deformation mechanism is negative; when the thickness is less than the threshold, deformation mechanism is positive.

A finite element simulation proved that as the specimen is thoroughly strained, positive bending angle forms; as the ratio of depth of the laser pulse-induced plastic deformation and the specimen thickness decreases to significantly less than 1, negative bending takes place. Positive bending angle is critically affected by the laser process parameters when the specimen thickness is thin. An empirical correlation equation was obtained by multiple regressions based on the positive bending experiments. This regression showed that the bending angle rises with the increase of overlapping ratio, passes of tracks, and laser pulse power intensity, and decreases with the specimen thickness [6].

CHAPTER V

PATTERNING USING HIGH ENERGY PULSE LASER PEENING FOR BIO-

APPLICATIONS

Introduction

In this chapter, the HEPLP process is investigated to introduce innovative micro-patterns and surface enhancement on cpTi samples within a one-step process. The approach is based on the simultaneous experimental and numerical investigation of the process. A cell culture test is then conducted on the patterned area to investigate the contribution and effect on the attached cell density, cell growing mode, and cell attachment location of the 2D patterns. However, first the need for the micro-patterns are described in the section below.

Current Issues for Bio-Implants

One major issue with dental implant devices is the chronic inflammation due to the lack of tissue growth around the implant device, which can lead to the potential for mucosal recession or even implant loss. Studies have shown that the microtopography of the surface that the cells attach to is a factor in cell-attachment to dental implant devices. In addition, it has been found that a grooved or roughened surface contributes to the osteoblast differentiation in human mesenchymal pre-osteoblastic cells, which helps to avoid long-term peri-abutment inflammation issues for the dental implant therapy with transcutaneous devices. When comparing rough versus grooved surfaces, it has been seen that the cells align with the grooves on the grooved surface, and similarly with the pattern found on the rough surface [36,37,39,40]. However, existing approaches, such as grit blasting, acid etching, or uni-directional grooving of Ti surfaces, can damage the implant and the surface quality is very difficult to control.

Another issue in the bio-industry is that titanium alloys, such as Ti-6Al-4V, are commonly used as biomedical implants because of their superior mechanical properties to

pure titanium, however there is a risk of leeching toxic alloy elements into the body which can lead to long term health effects [39,40]. Due to this, pure titanium is the preferred material for these applications; however, it has limited mechanical strength, and the implants often fail due to the coupled effects of corrosion, fatigue and fracture under cyclic loading and high stresses in such an aggressive environment [49–52]. Detailed analyses have shown that about 60% of the failed titanium implant plates has occurred through corrosion fatigue, which was promoted by the presence of intense localized corrosion and intergranular cracking [9]. Corrosion, the gradual degradation of materials by electrochemical attack, is of great concern, particularly when a metallic implant is placed in the hostile electrolytic environment of the human body [53]. Metal fatigue, a process in which repeated stressing causes cracking and failure, is found to get further accelerated due to corrosion as well as the formation of wear debris leading to fatigue wear. On the other hand, during fatigue there is disruption of the oxide layer and the inability of the material to repassivate immediately exposes some region of the metal to the environment, leading to corrosion. As a material starts to corrode, the dissolution of metal will lead to erosion which in turn will eventually lead to brittleness and fracture of the implant. Once the material fractures, corrosion accelerates due to an increase in the amount of exposed surface area and loss of protective oxide layer [39,40]. Corrosive fatigue can occur in titanium hip implants by simply walking, which causes cyclic loading at a frequency of about 1 Hz [54]. If the metal fragments from the damaged implant are not surgically extracted, further dissolution and fragmentation can occur, which may result in inflammation of the surrounding tissues [9].

While micro-patterning is the key objective to this investigation, by using the HEPLP process to do this, the material can also benefit from the conventional advantages of the HEPLP process. Advantages to the HEPLP process were described in greater detail

in Chapter II and include increased strength, hardness, and corrosion resistance from the refined grain structure that HEPLP induces.

Setup and Experiments

For the experimental portion of this chapter, the implant material is first patterned using the HEPLP process. After the pattern is imprinted, cell attachment experiments are conducted to validate the improvements in cell attachment to a patterned surface verses a non-patterned surface.

<u>Patterning of Bio-Implant Material</u>

In this study, HEPLP was applied to imprint a pattern, consisting of 20 μm grooves, into the dental implant material, cpTi. The experiments consisted of a 200 grid TEM mesh (Figure 22), BK7 glass, and 13 μm thick cpTi foil. The mesh grid was "sandwiched" between two pieces of the Ti foil. The top Ti foil layer, cut to 6x6 mm2 was placed directly over the TEM mesh and was used as the ablative, "sacrificial" layer. The bottom Ti layer, was used as the patterned surface, as it is free for thermal damage from the laser, and was later used for the cell culture tests. As shown in Figure 21, the 2x2 in2 glass was placed on both sides of the titanium foil "sandwich", acting as the confinement layer [55].
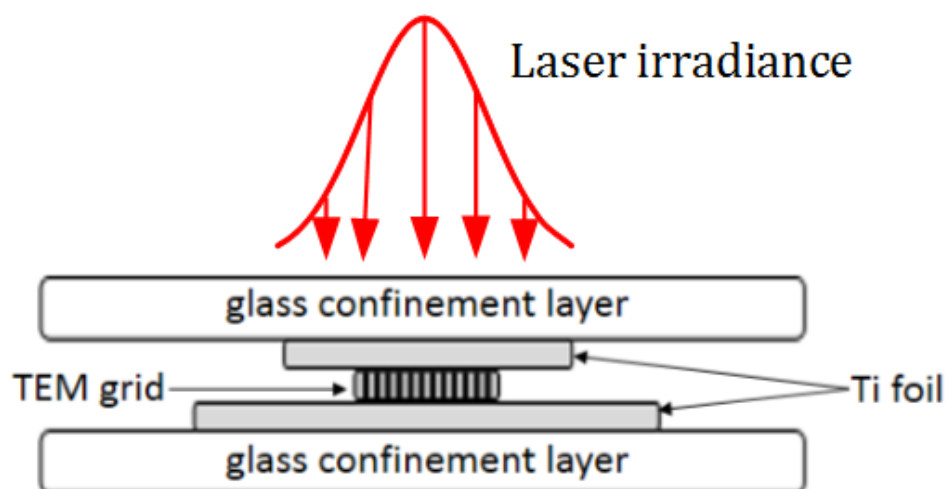

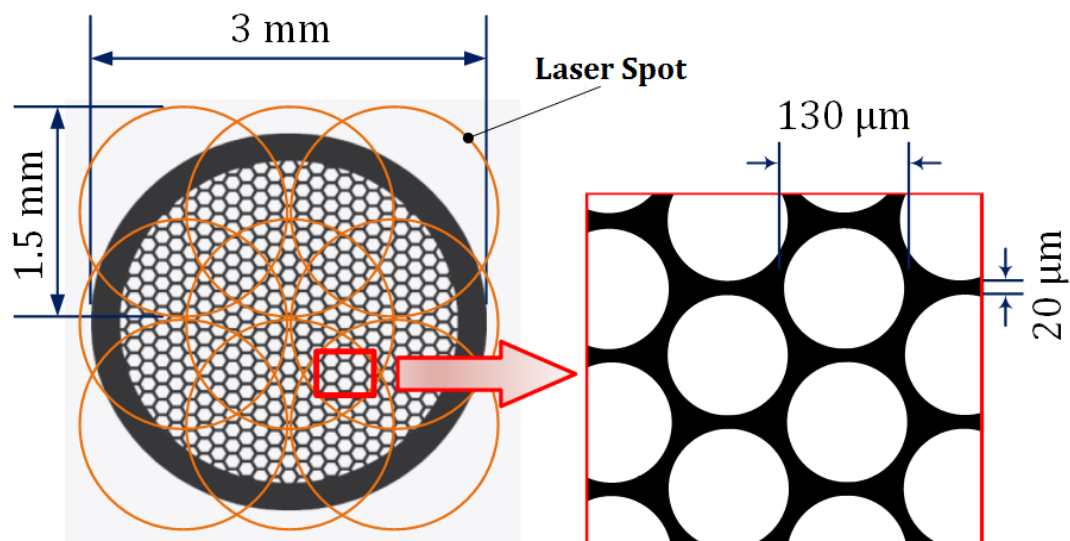Figure 21. The experimental setup for the grid imprinting.

Figure 22. The 3x3 laser spot matrix on the pattern mask with dimensions of the pattern mask and laser spots.

Next, a 3×3 matrix of laser pulses 1.24 mm in diameter was shot in alignment with the top "sacrificial" piece of titanium foil, as shown in Figure 21 and Figure 22. The pulses were delivered by a Q-switched Nd-YAG laser (8 ns pulse duration, 1064 wavelength) at a power density of 3.21 GW/cm^2. The bottom piece of titanium foil was used for the cell culture tests, as this piece will have an undamaged imprint of the TEM mesh. Table 5 shows the laser parameters used for the patterning portion of the experiment, these were varied until an optimal set of parameters were found. This optimal set was classified as producing a pattern with the deepest imprint in the bottom piece of Ti foil [55].

Table 5. Patterning experimental parameters

Parameter	Value
Pulse energy (mJ)	380
Beam Size (mm)	1.24
Power Density (GW/cm^2)	3.21
Pulse Duration (ns)	8
TEM Grid Dimensions (μm)	200 Grid Mesh: Thickness: ~12 Hole diameter: 130 Minimum bar width: 20

The patterned cpTi samples were then studied using both a Hitachi S-4800 scanning electron microscope (SEM) and a Veeco Wyko NT1100 non-contact optical surface profilmeter. From these tools, both two-dimensional and three-dimensional surface plots were created and analyzed (Figure 23 and Figure 24). Figure 23 and Figure 24 show that the pattern from the TEM mesh was successfully imprinted onto the Ti surface, and Figure 24b was used to find the depth of the grooved portion of the pattern. The grooved area is shown in Figure 22, where the grooves are the black area between the white circles (within the red boxed area), and are roughly 20 μm in width. The grooved area also corresponds to the blue area in Figure 24. After taking 10 surface profilmeter images, the deepest imprinted goove was roughly 7 μm, with an average depth of 5.92 μm and standard deviation of 1.32 μm.

Figure 24 also shows deformation results from a fully coupled thermo-mechanical ABAQUS/Explicit analysis of the patterning process. The analysis is simplified to two-dimensional and is carried out for one patterned indentation to reduce computational cost. It is also considered axisymmetric, with the axis postioned at the center of one of the

patterned indentations of the cpTi. The simulation domain is shown in the red dashed box in Figure 24. The laser-induced shock wave pressures predicted by hydrodynamics model were applied as user-defined distributed time-dependent pressure loads in ABAQUS. At the indentation, the maximum deformation is roughly 8 μm, which compares well with the results from the surface profilmeter.
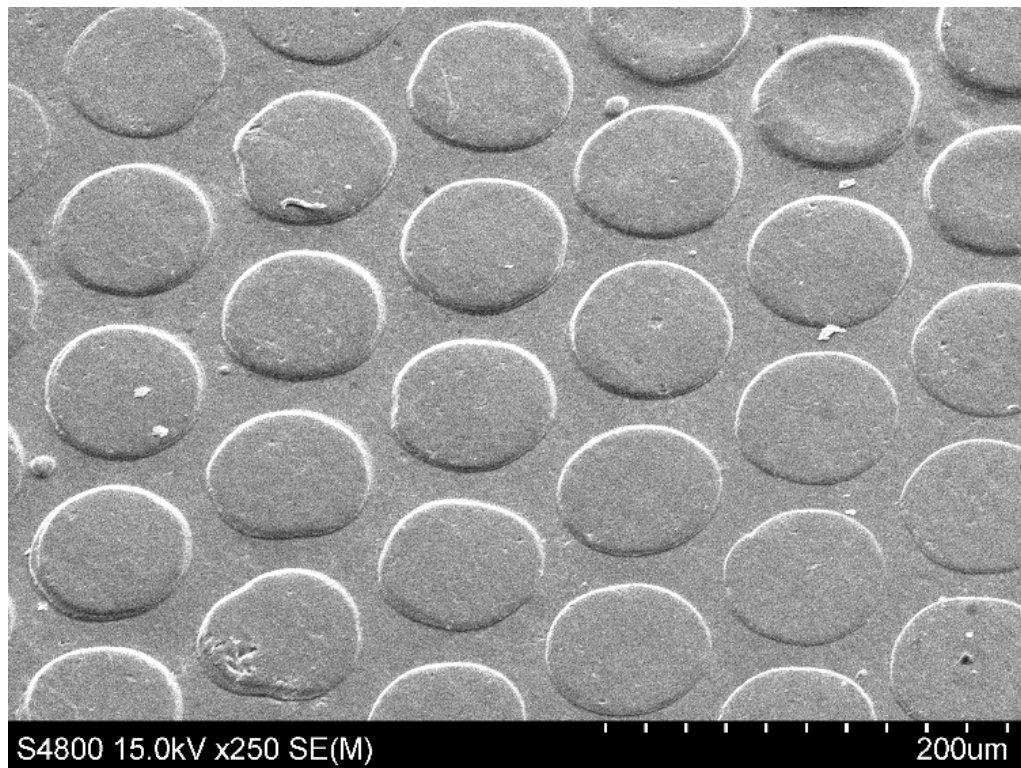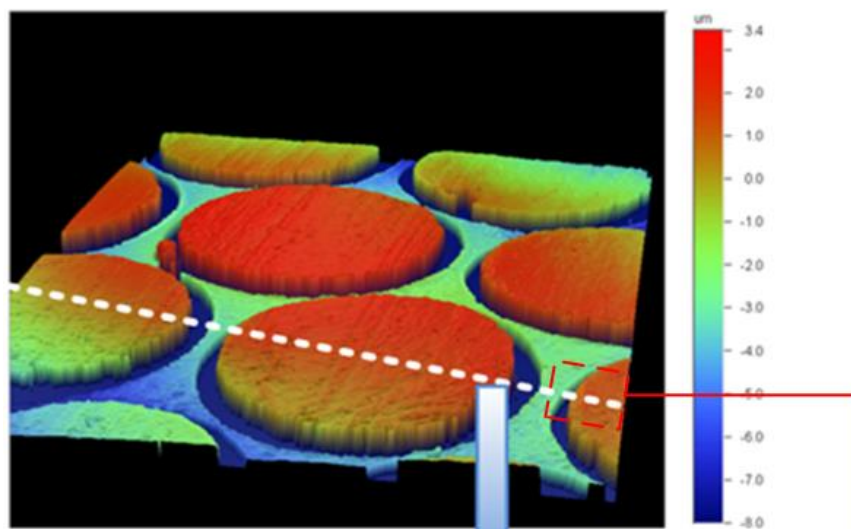

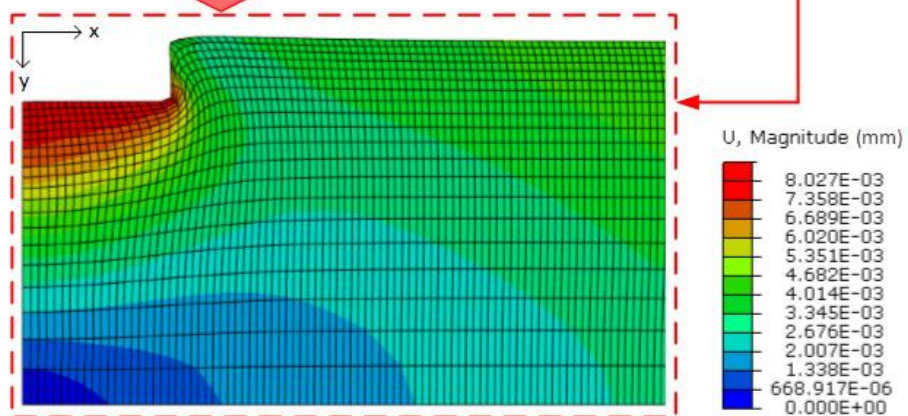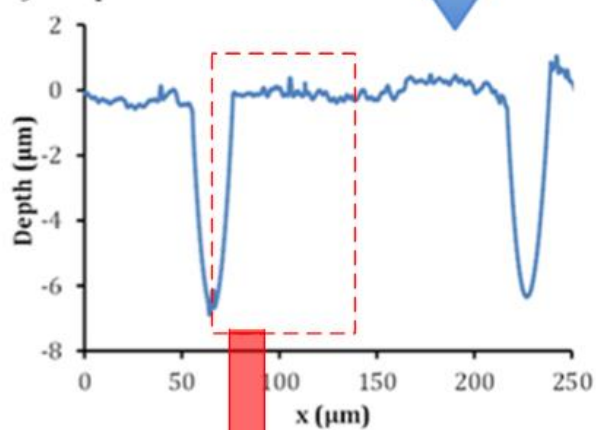Figure 23. SEM image of the patterned cpTi surface.

a) 3D map

b) 2D profile

Figure 24. Surface profile and FEA results of the patterned cpTi surface.

Cell Culture

After patterning and analyzing the cpTi surfaces, cell culture tests were completed in collaboration with Yin Yu from Professor Ibrahim Ozbolat's lab to draw conclusions on the possible improvements in cell attachment to the imprinted implant surface, from the previous section, rather than a smooth surface. Upon the scale of the width of the channel, bovine chondrocytes were used in the cell attachment study, which are usually 10-20 µm in diameter. Basically, chondrocytes were harvested by collagenase and protease. Then cells were cultured at culture vessels in Dulbecco`s modified Eagle`s medium (DMEM) supplemented with 10% fetal bovine serum (Invitrogen Life Technologies), 50 µg/ml L-ascorbate, 100 units/ml penicillin, 100 µg/ml streptomycin, and 2.5 µg/ml Fungizone at 37° C in 5% CO_2. Cell culture media was replenished every other day, where passage 1 chondrocytes were used in this study. Cells were seeded at a density of 500,000/mL media for all experimental groups [55].

Implant samples were sterilized with UV light for 24 hours, and pre-equilibrated in the cell culture media overnight. Before cell seeding, samples were set in a biosafety cabinet for completely dry air. Upon cell seeding, samples were kept in the incubator on a flat surface, and cultured at 37 °C in 5% CO_2. Figure 25 shows a sample submerged in the cell culture media and kept in a Sanyo cell incubation chamber. Patterned foil samples were attached to copper cylinders for easier handling [55].

Figure 25. Patterned cpTi foil fixed on a copper cylinder fixture seeded with
chondrocytes in a cell culture chamber for cell incubation.

After the cell culture test, the samples were removed from the incubator and
immediately sent for cell fixation, dehydration, and sputter coating for SEM imaging. The
cell media was aspirated, and then 1 mL of Phosphate-Buffered Saline (PBS) washed over
the samples and was removed twice. At that point, the cells were fixed in the two step
process: a) the crosslinking fixation for 1 hour, and b) oxidizing fixation for 30 min. In the
crosslinking fixation, covalent chemical bonds were created between proteins in the tissue,
which anchored the soluble proteins to the cytoskeleton for additional rigidity. The fixative
agent in the first step, 3% Gluteraldehyde-3% Formaldehyde, was applied and removed
after 30 minutes. Before the second step, a 0.1 M Sodium Cacodylate Buffer was placed in
the washed over the foil, then removed, and then repeated one additional time (4 min for
each time). Next, the 1% Osmium tetroxide (OsO4) in buffer was applied in the second
setup. The oxidizing fixatives, such as OsO4, can react with various side chains of proteins,

fats and other biomolecules, allowing for the formation of crosslinks that stabilize a tissue structure. In addition, OsO₄ is often used as a secondary fixative when samples are prepared for electron microscopy. The 1% Osmium tetroxide in buffer was made by mixing 2 parts of 0.2 M Sodium Cacodylate Buffer, 1 part of 4% OsO4 solution, and 1 part of deuterium-depleted water (dd water) [55].

Following the fixation, the samples were rinsed using dd water twice and then dehydrated with ethanol solutions. The samples were placed in solution with 30%, 50%, 70%, 95%, and lastly twice with 100% ethanol for 10 minutes. The chemical drying was conducted twice (10 min for each time) with Hexamethyldisilazane (HMDS) to prevent the shrinkage and collapse of surface structures, which can happen due to the effects of surface tension when a biological sample is air dried following dehydration. Then, a thin layer of gold and platinum was sputtered on the whole surface of the Ti foils in a K500 EMItech sputter coater for 3 min, to enhance the secondary electrons backscattered [55].

Experimental Results

Figure 26 shows the comparison of the attached cell density between the patterned area and original flat surface. The patterned area appeared to have significantly higher cell density than that on the original flat surface of the Ti foil, especially in the channel. Despite of the help on the cell density, Figure 27 shows the effect of imprinted channels on the cell growing mode and cell attachment location.

a) Patterned area
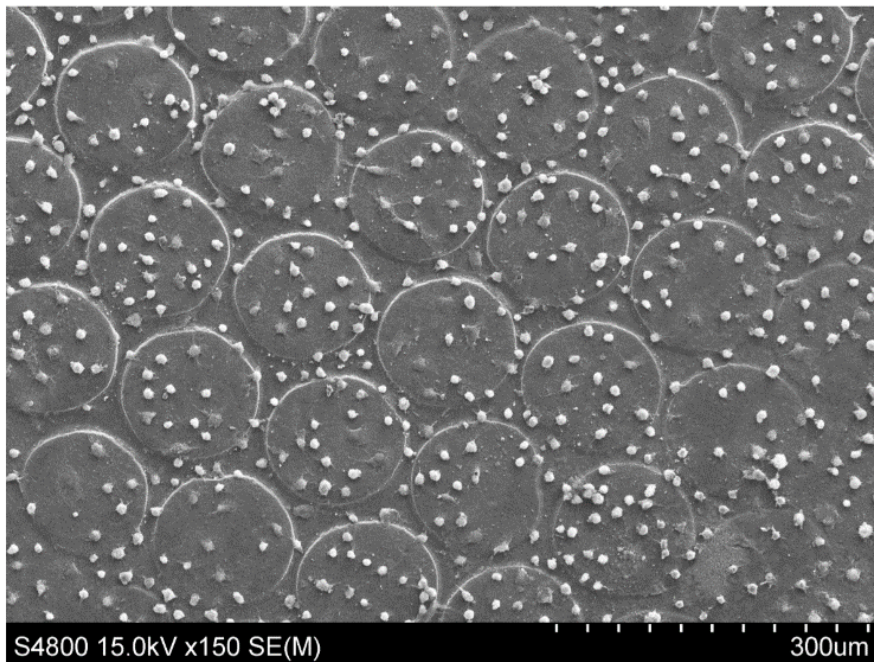
b) Original flat surface
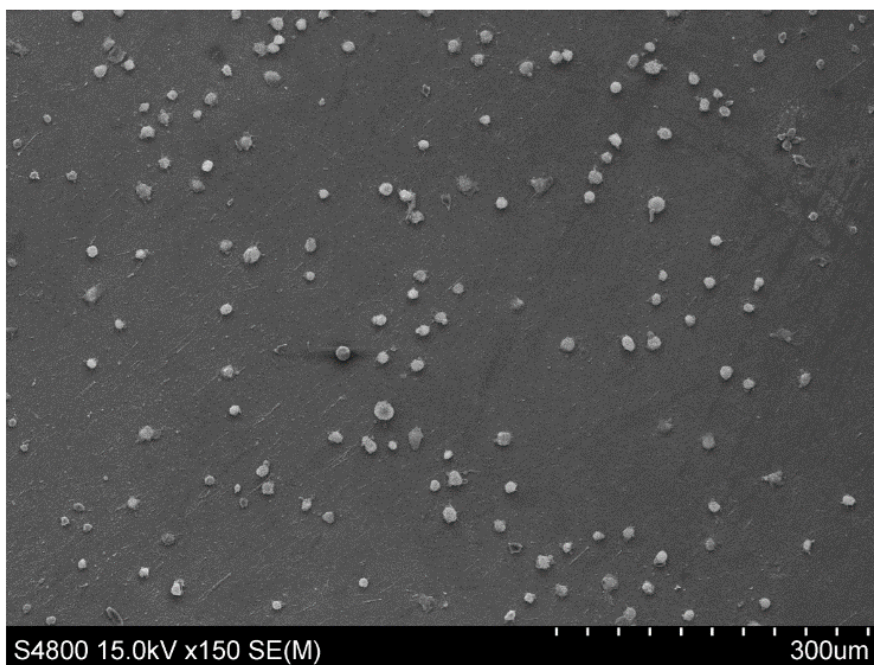
Figure 26. Comparison of SEM images of the patterned area (a) and the original flat surface (b) of the cpTi foil after cell culture tests.

a) Zoomed-in view in the channel
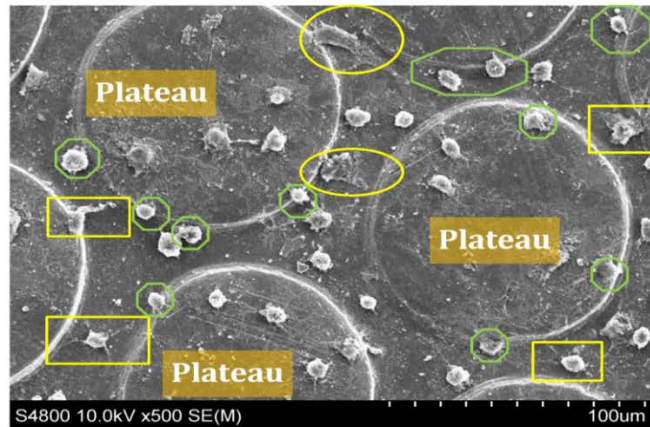
b) An outgrowing cell in the channel
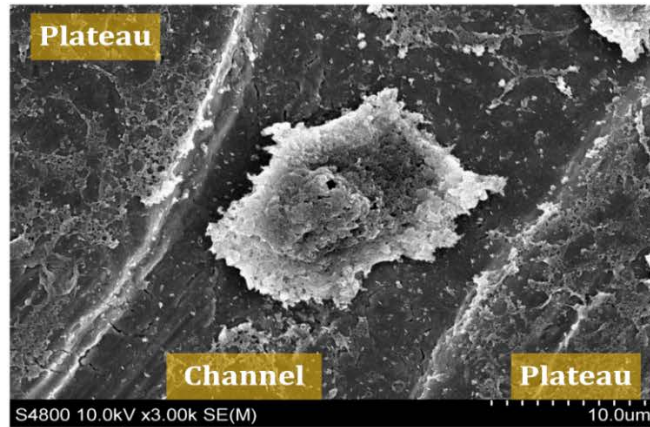
c) A no-outgrowth cell attached on the flat surface

Figure 27. Different cell growing modes from the patterned area to the original flat surface. In (a), the outgrown (ellipse), outgrowing cells (rectangle) in the channel and cells sitting on the wall of the channel (octagon) are highlighted.

There were two essential cell growing modes, outgrowth and no-outgrowth, which can be seen in this cell culture test. Cells sitting in the channel, especially in the neck of a channel (minimum width), usually tried to reach the wall of the channel. These cells appeared in different growth stages due to different growing speeds. In Figure 27a, completely outgrown and outgrowing cells are highlighted with yellow elliptical circles and rectangular boxes, respectively. Nevertheless, the cells that attached to the flat surface still have a spherical shape (Figure 27c), which usually corresponds to a poorer cell attachment. Figure 27b clearly shows an outgrowing cell located in the neck of a channel. The cell was trying to stretch to touch the wall of the channel on the both sides. Thus, the imprinted channel can also help the attached cell growth, not only the cell attachment. However, the outgrowth can hardly been seen with the cells located on the three adjacent plateaus, due to the fairly wide and open area. Cells located on these plateaus were similar to those attached to flat surface, which also appeared no-outgrowth. Therefore, the effect of imprinted channels on the cell growth is more dominated by the width of the channel than the depth. To enhance this effect, the channel width should be comparable to the cell size. In this study, the width of the neck of channel is 20 µm, while the cell size is about 10-20 µm.

In addition, cells would like to accommodate themselves in the corner of the channel as well. The cells located in the corners are highlighted with the light green octagonal boxes in Figure 27a. This helped the cell attachment in the patterned area even further.

Conclusion

From the experiments conducted in this study, it was shown that patterns can be imprinted on the dental implant material, cpTi, with the novel technique of HEPLP. Simulation results using the physics-based hydrodynamic modeling results from Chapter III as loading conditions, were able to accurately predict the depth of the patterned grooves.

Comparing the experimental and simulated results from ABAQUS, the depth of grooves from experiments were about 6-7 µm, while the ABAQUS results produced a groove depth of about 8 µm.

The techniques were not only successful at roughening the surface topology of the cpTi, but also creating a patterned surface, which is helpful to obtain a higher cell density in the cell-attachment test. Roughening of the surface topology is believed to contribute to the osteoblast differentiation in human mesenchymal pre-osteoblastic cells, which helps to avoid long-term peri-abutment inflammation issues for the dental implant therapy with transcutaneous device. Existing approaches, such as the grit blasted, acid etched, or uni-directional grooved Ti surfaces, can damage the implant and the surface quality is very difficult to control. The new approach can eliminate both of these issues.

Besides the increase in cell attachment, improvements in cell growth and cell attachment location were also demonstrated. In this study, cells located in the channel, especially in the neck of a channel (minimum width), usually tried to expand to reach the walls of the channel, which resulted in the outgrowth of a cell. Cells attached on the flat surface maintain their spherical shape, which usually refers to a poorer cell attachment. The width of the channel is more critical than its depth in this study. The outgrowth can hardly been seen at the location among three adjacent plateaus due to the fairly wide and open area. Cells sitting here were not too much different from those attached on a flat surface appearing no-outgrowth. Therefore, the effect of imprinted channels on the cell growth is determined by the width more than the depth. To enhance this effect, the channel width should be comparable to the cell size. In future work, a square stamp with uniform bar width around 20-30 µm is expected to generate a more cell friendly pattern. If there are any options in which the channel width can be less than 10 µm, it would be preferred to match the oral tissue cell size, which is more relevant to this study. In addition, cells would

like to accommodate themselves in the corner of the channel, which added to the increase in cell attachment in the patterned area.

CHAPTER VI

CONCLUSION

Overall, it was shown that the multi-physics based hydrodynamic model presented in Chapter III could successfully predict the pressures induced on the surface during the HEPLP process, which was then used to accurately predict bending in Chapter IV and the depth of the patterned grooves in Chapter V.

In Chapter IV, covering sheet metal bending using HEPLP, it was concluded that the deformation of the laser micro-bending was determined with the specimen thickness and laser energy. From the test results, it was shown that with the same laser parameters, the thickness of the specimen is the dominant factor in determining the deformation mechanism. Comparing the thickest specimen of 1.75 mm and the thinnest specimen of 0.25 mm, it's clear that the thinner sheet will deform in the positive direction, while the thicker sheets will deform in the negative direction, under all laser energy conditions. The transition thickness, where the bending mechanism changes from positive to negative, was determined to be 0.7-0.88 mm. The laser energy has more significant effects with thinner specimen, contributing to a greater positive deformation. However, the laser energy is has little effect on bending angle of thicker sheets (negative deformation mechanism).

Chapter V showed that the HEPLP process could be a promising technique in the bio-implant industry, increasing cell-attachment on dental implant material by creating surface micro-patterns with the technique. It was found that the effect of imprinted channels on the cell growth is determined by the width more than the depth. Also, the channel width should be comparable to the cell size to enhance the effectiveness.

REFERENCES

[1]   Wu B., and Shin Y. C., 2007, "A one-dimensional hydrodynamic model for pressures induced near the coating-water interface during laser shock peening," J. Appl. Phys., **101**(2), p. 023510.

[2]   Ding H., and Shin Y. C., 2012, "Dislocation density-based modeling of subsurface grain refinement with laser-induced shock compression," Comput. Mater. Sci., **53**(1), pp. 79–88.

[3]   Cao Y., Shin Y. C., and Wu B., 2010, "Parametric Study on Single Shot and Overlapping Laser Shock Peening on Various Metals via Modeling and Experiments," J. Manuf. Sci. Eng., **132**(6), p. 061010.

[4]   Wu B., and Shin Y. C., 2007, "Two dimensional hydrodynamic simulation of high pressures induced by high power nanosecond laser-matter interactions under water," J. Appl. Phys., **101**(10), p. 103514.

[5]   Ye C., and Cheng G. J., 2012, "Scalable patterning on shape memory alloy by laser shock assisted direct imprinting," Appl. Surf. Sci., **258**(24), pp. 10042–10046.

[6]   Pence C., Ding H., Shen N., and Ding H., 2013, "Experimental analysis of sheet metal micro-bending using a nanosecond-pulsed laser," Int. J. Adv. Manuf. Technol., **69**(1-4), pp. 319–327.

[7]   Kumar S., and Narayanan T. S. N. S., 2008, "Corrosion behaviour of Ti-15Mo alloy for dental implant applications.," J. Dent., **36**(7), pp. 500–7.

[8]   Singh R., and Dahotre N. B., 2007, "Corrosion degradation and prevention by surface modification of biometallic materials.," J. Mater. Sci. Mater. Med., **18**(5), pp. 725–51.

[9]   Thalji G., Gretzer C., and Cooper L. F., 2013, "Comparative molecular assessment of early osseointegration in implant-adherent cells.," Bone, **52**(1), pp. 444–53.

[10]   Antunes R. A., and de Oliveira M. C. L., 2012, "Corrosion fatigue of biomedical metallic alloys: mechanisms and mitigation.," Acta Biomater., **8**(3), pp. 937–62.

[11]   Ding H., Shen N., and Shin Y. C., 2012, "Predictive modeling of grain refinement during multi-pass cold rolling," J. Mater. Process. Technol., **212**(5), pp. 1003–1013.

[12]   Ding H., Shen N., and Shin Y. C., 2011, "Modeling of grain refinement in aluminum and copper subjected to cutting," Comput. Mater. Sci., **50**(10), pp. 3016–3025.

[13] Fabbro R., Fournier J., Ballard P., Devaux D., and Virmont J., 1990, "Physical study of laser-produced plasma in confined geometry," J. Appl. Phys., **68**(2), p. 775.

[14] Peyre P., Chaieb I., and Braham C., 2007, "FEM calculation of residual stresses induced by laser shock processing in stainless steels," Model. Simul. Mater. Sci. Eng., **15**(3), pp. 205–221.

[15] Amarchinta H. K., Grandhi R. V., Clauer A. H., Langer K., and Stargel D. S., 2010, "Simulation of residual stress induced by a laser peening process through inverse optimization of material models," J. Mater. Process. Technol., **210**(14), pp. 1997–2006.

[16] Braisted W., and Brockman R., 1999, "Finite element simulation of laser shock peening," Int. J. Fatigue, **21**(7), pp. 719–724.

[17] Hu Y., Yao Z., and Hu J., 2006, "3-D FEM simulation of laser shock processing," Surf. Coatings Technol., **201**(3-4), pp. 1426–1435.

[18] Achintha M., and Nowell D., 2011, "Eigenstrain modelling of residual stresses generated by laser shock peening," J. Mater. Process. Technol., **211**(6), pp. 1091–1101.

[19] Wu B., and Shin Y. C., 2005, "A self-closed thermal model for laser shock peening under the water confinement regime configuration and comparisons to experiments," J. Appl. Phys., **97**(11), p. 113517.

[20] Liu J., Sun S., Guan Y., and Ji Z., 2010, "Experimental study on negative laser bending process of steel foils," Opt. Lasers Eng., **48**(1), pp. 83–88.

[21] Guan Y., Zhang H., Liu J., and Sun S., 2012, "Laser micro-bending process based on the characteristic of the laser polarization," J. Mater. Process. Technol., **212**(3), pp. 662–671.

[22] Geiger M., and Vollertsen F., 1993, "The mechanisms of laser forming," CIRP Ann Manuf Technol, **42**(1), pp. 301–304.

[23] Shen H., Hu J., and Yao Z., 2010, "Analysis and control of edge effects in laser bending," Opt. Lasers Eng., **48**(3), pp. 305–315.

[24] Everett R. A., Matthews W. T., Directorate V. T., and Prabhakaran R., 2001, The Effects of Shot and Laser Peening on Fatigue Life and Crack Growth in 2024 Aluminum Alloy and 4340 Steel, National Aeronautics and Space Administration, Langley Research Center, Hampton, Va; Hanover, MD.

[25] Li J., Gao H., and Cheng G. J., 2010, "Forming Limit and Fracture Mode of Microscale Laser Dynamic Forming," J. Manuf. Sci. Eng., **132**(6), p. 061005.

[26] Ye C., and Cheng G. J., 2010, "Effects of Temperature on Laser Shock Induced Plastic Deformation: The Case of Copper," J. Manuf. Sci. Eng., **132**(6), p. 61009.

[27] Safdar S., Li L., and Sheikh M. a., 2007, "Finite element simulation of laser tube bending: Effect of scanning schemes on bending angle, distortions and stress distribution," Opt. Laser Technol., **39**(6), pp. 1101–1110.

[28] Wielage H., and Vollertsen F., 2011, "Classification of laser shock forming within the field of high speed forming processes," J. Mater. Process. Technol., **211**(5), pp. 953–957.

[29] Shidid D. P., Gollo M. H., Brandt M., and Mahdavian M., 2013, "Study of effect of process parameters on titanium sheet metal bending using Nd: YAG laser," Opt. Laser Technol., **47**, pp. 242–247.

[30] Maji K., Pratihar D. K., and Nath a. K., 2013, "Experimental investigations and statistical analysis of pulsed laser bending of AISI 304 stainless steel sheet," Opt. Laser Technol., **49**, pp. 18–27.

[31] Hoseinpour Gollo M., Mahdavian S. M., and Moslemi Naeini H., 2011, "Statistical analysis of parameter effects on bending angle in laser forming process by pulsed Nd:YAG laser," Opt. Laser Technol., **43**(3), pp. 475–482.

[32] Geiger M., and Meyer-Pittroff F., 2002, "Laser beam bending of metallic foils," pp. 187–190.

[33] Edwardson G. D. and S. P., 2003, "Some recent developments in two-and three-dimensional laser forming for 'macro' and 'micro' applications," J. Opt. A Pure Appl. Opt., **5**(4), p. S8.

[34] Zhang X. R., and Xu X., 2005, "Laser bending for high-precision curvature adjustment of microcantilevers," Appl. Phys. Lett., **86**(2), p. 021114.

[35] Zhang X. R., and Xu X., 2005, "Laser bending for adjusting curvatures of hard disk suspensions," Microsyst. Technol., **11**(11), pp. 1197–1203.

[36] Masaki C., Schneider G. B., Zaharias R., Seabold D., and Stanford C., 2005, "Effects of implant surface microtopography on osteoblast gene expression.," Clin. Oral Implants Res., **16**(6), pp. 650–6.

[37] Schneider G. B., Zaharias R., Seabold D., Keller J., and Stanford C., 2004, "Differentiation of preosteoblasts is affected by implant surface microtopographies.," J. Biomed. Mater. Res. A, **69**(3), pp. 462–8.

[38]   Schneider G. B., Zaharias R., Seabold D., Keller J., and Stanford C., 2004, "Differentiation of preosteoblasts is affected by implant surface microtopographies.," J. Biomed. Mater. Res. A, **69**(3), pp. 462–8.

[39]   Subramani K., and Mathew R. T., 2012, Chapter 6. Titanium Surface Modification Techniques for Dental Implants—From Microscale to Nanoscale, Elsevier Inc., Boston.

[40]   Subramanian K., Tran D., and Nguyen K. T., 2012, Chapter 8. Cellular Responses to Nanoscale Surface Modifications of Titanium Implants for Dentistry and Bone Tissue Engineering Applications, Elsevier Inc., Boston.

[41]   Pedrotti F. L., and Pedrotti L. S., 1993, Introduction to Optics, Prentice Hall, Englewood Cliffs, NJ.

[42]   Lee Y. T., and More R. M., 1984, "An electron conductivity model for dense plasmas," Phys. Fluids, **27**(5), p. 1273.

[43]   Ree F. H., 1976, Report No. UCRL-52190 (unpublished), Livermore, Calif.

[44]   More R. M., Warren K. H., Young D. a., and Zimmerman G. B., 1988, "A new quotidian equation of state (QEOS) for hot dense matter," Phys. Fluids, **31**(10), p. 3059.

[45]   Liu X., and Osher S., 1998, "Convex ENO High Order Multi-dimensional Schemes without Field by Field Decom- position or Staggered Grids," J. Comput. Phys., **141**, pp. 1–27.

[46]   Peyre P., Berthe L., Fabbro R., and Sollier A., 2000, "No Title," J. Phys. D, **33**, p. 498.

[47]   Montross C., 2002, "Laser shock processing and its effects on microstructure and properties of metal alloys: a review," Int. J. Fatigue, **24**(10), pp. 1021–1036.

[48]   Hua D., Yun W., and Lan C., 2010, "Laser shock forming of aluminum sheet: Finite element analysis and experimental study," Appl. Surf. Sci., **256**(6), pp. 1703–1707.

[49]   Rack H. J., and Qazi J. I., 2006, "Titanium alloys for biomedical applications," Mater. Sci. Eng. C, **26**(8), pp. 1269–1277.

[50]   Liu X., Chu P., and Ding C., 2004, "Surface modification of titanium, titanium alloys, and related materials for biomedical applications," Mater. Sci. Eng. R Reports, **47**(3-4), pp. 49–121.

[51] Metikoš-Huković M., Kwokal a, and Piljac J., 2003, "The influence of niobium and vanadium on passivity of titanium-based implants in physiological solution," Biomaterials, **24**(21), pp. 3765–3775.

[52] Aksakal B., Yildirim Ö. S., and Gul H., 2004, "Metallurgical Failure Analysis of Various Implant Materials Used in Orthopedic Applications," J. Fail. Anal. Prev., **4**(3), pp. 17–23.

[53] Kumar S., and Narayanan T. S. N. S., 2008, "Corrosion behaviour of Ti-15Mo alloy for dental implant applications.," J. Dent., **36**(7), pp. 500–7.

[54] Singh R., and Dahotre N. B., 2007, "Corrosion degradation and prevention by surface modification of biometallic materials.," J. Mater. Sci. Mater. Med., **18**(5), pp. 725–51.

[55] Shen N., Pence C., Bowers R., Yu Y., Ding H., Stanford C., and Ozbolat I., 2014, "Surface Micro-scale Patterning for Biomedical Implant Material of Pure Titanium via High Energy Pulse Laser Peening," ASME, ed., Detroit, Michigan, pp. 1–7.